Experimental characterisation and finite element modeling of biodegradable magnesium stents

Arnout Oppeel

Supervisors: Prof. dr. ir. Benedict Verhegghe, Prof. dr. Peter Dubruel
Counsellor: Ir. Nic Debusschere

Master's dissertation submitted in order to obtain the academic degree of
Master of Science in Biomedical Engineering

Department of Electronics and Information Systems
Chairman: Prof. dr. ir. Jan Van Campenhout

WE07
Chairman: Prof. dr. José Martins

Faculty of Engineering and Architecture
Academic year 2014-2015

UNIVERSITEIT GENT

Experimental characterisation and finite element modeling of biodegradable magnesium stents

Arnout Oppeel

Supervisors: Prof. dr. ir. Benedict Verhegghe, Prof. dr. Peter Dubruel
Counsellor: Ir. Nic Debusschere

Master's dissertation submitted in order to obtain the academic degree of
Master of Science in Biomedical Engineering

Department of Electronics and Information Systems
Chairman: Prof. dr. ir. Jan Van Campenhout

WE07
Chairman: Prof. dr. José Martins

Faculty of Engineering and Architecture
Academic year 2014-2015

UNIVERSITEIT GENT

Acknowledgements

Writing this dissertation as the finale of my engineering studies would not have been possible without the support from several people.

Firstly, I would like to thank Matthieu De Beule and Nic Debusschere (ELIS-bioMMeda) for taking the time to introduce to me the basic concepts of stent finite element modeling and for being available on a daily basis. Thanks to their guidance, I was able to work on this topic with ever-increasing independence. Nic, I hope that the study I have done can constitute a small contribution to the validation of your research. Next, I thank Prof. Benedict Verhegghe and Prof. Patrick Segers for their expert opinions. Even more, the pyFormex software and the BuMPer cluster, both created by Prof. Verhegghe, prove to be the driving resources of FE stent modeling.

I would also like to thank Prof. Peter Dubruel and the members of the Polymer Chemistry and Biomaterials Group (PBM) for providing access to the laboratory equipment.

My gratitude also goes to Prof. Joris Degrieck and Ives De Baere (Department of Materials Science and Engineering) for the guidance they provided with regard to mechanical testing of metallic materials.

Last, but not least, I am very grateful to my family and Margot for their patience and support throughout my entire academic education.

Arnout Oppeel
Ghent, May 2015

Experimental characterisation and finite element modeling of biodegradable magnesium stents

by Arnout Oppeel

Master of Science in Biomedical Engineering

UNIVERSITEIT GENT
Faculty of Engineering and Architecture
Department of Electronics and Information Systems

Abstract

In this work, concepts in areas like finite element modeling, materials science and chemistry are brought together in order to validate the suitability of the developed framework for the modeling of biodegradable magnesium stents. Corrosion experiments are carried out with the intention to calibrate the model parameters based on the collected data. Once properly calibrated, the corrosion model is applied to simulate the deployment and degradation of a realistic magnesium stent.

In the introductory Chapter 1, both the possible benefits and limitations of degradable stents compared to permanent devices are explored. The main design requirements are also described. Chapter 2 provides an extensive review of the literature on stent magnesium alloy corrosion. The chapter deals with the specific corrosion mechanism that is observed for such alloys, protocols for immersion and electrochemical in vitro testing and quantitative evaluation of the corrosion rate. Next, the state of the art of computational corrosion modeling is reviewed. The aim of the experiments outlined in Chapter 3 is to evaluate the in vitro corrosion rate of the Mg AZ31 alloy, the effect of corrosive degradation on the mechanical properties and the effect of loading on the corrosion process. The architecture of the continuum damage mechanics corrosion modeling framework is given in Chapter 4. The phenomenological evolution laws governing pitting and stress corrosion are discussed, as well as the implementation by means of a user subroutine (UMAT) compatible with the commercial FE solver Abaqus/Standard. The calibrated corrosion model is applied to the FE modeling of realistic stent mechanics in Chapter 5. It is checked whether the proposed approach is suitable to predict stent mechanics, as well as degradation. Finally, conclusions and considerations for future work in the field of degradable stent modeling are given in Chapter 6.

Experimental characterisation and finite element modeling of biodegradable magnesium stents

Arnout Oppeel

Supervisor(s): Benedict Verhegghe, Peter Dubruel, Matthieu De Beule, Nic Debusschere

Abstract— **A continuum damage mechanics framework has been developed in order to model magnesium alloy stent corrosion. Both pitting and stress corrosion are implemented in the finite element (FE) scheme. The corrosion model is calibrated for the magnesium AZ31 alloy, based on experimental data collected from degradation experiments and mechanical tests. Eventually, the corrosion modeling framework is applied to the FE modeling of realistic biodegradable stent mechanics.**

Keywords— **Biodegradable stent, magnesium alloy, finite element modeling, corrosion model**

I. Introduction

THE current generation bare metal and drug eluting stents have significantly improved the prognosis of coronary artery disease treatment. However, permanent stent devices are associated with in-stent restenosis, thrombosis, delayed re-endothelialization and inflammation. Biodegradable stents show considerable promise with regard to alleviating these long-term complications. Furthermore, they do not form an obstruction for possible future minimally invasive interventions.

Ideally, the stent maintains its mechanical integrity for 6 to 12 months [1] to allow for the healing and remodeling of the diseased coronary artery. After this period, the device loses its radial strength and is resorbed completely by the human body. Both degradable polymers, such as poly-L-lactic acid (PLLA), and corrodible metal alloys, such as magnesium AZ31, constitute candidate stent materials. Polymers can be tailored to exhibit a well-defined degradational behaviour. Early clinical trial results for the Absorbable Metal Stent (AMS-1) developed by Biotronik [2] suggest good initial stiffness, but fast degradation and subsequent early loss of radial strength. To date, the biggest challenge in the design of biodegradable metallic stents is to achieve appropriate mechanical stability, without compromising biocompatibility.

Computational modeling has become an indispensable tool for design and virtual testing of endovascular devices. While numerical modeling of the mechanics of traditional non-degradable stents is a highly active field, much less modeling approaches have been reported to account for degrading stent material. One possible strategy is the explicit physical modeling of electrochemical corrosion reactions and transport processes. Another approach is application of continuum damage mechanics. The effects of corrosion on the structural integrity are then accounted for, without resorting to an explicit description of microscopic phenomena and their progression.

II. Mechanical alloy characterisation

A. Corrosive degradation mechanism

The corrosion properties of magnesium dictate those of the alloy. Corrosion of pure magnesium proceeds by an electrochemical reaction with water, producing magnesium hydroxide and hydrogen gas:

$$2\,Mg + 2\,H^+ + 2\,H_2O \longrightarrow 2\,Mg^{2+} + 2\,OH^- + 2\,H_2$$

In chloride containing solutions, such as body fluid, passivity is lost, as $Mg(OH)_2$ is converted into highly soluable $MgCl_2$. The partially protective $Mg(OH)_2$ layer is broken down, exposing the magnesium metal directly to the corrosive medium and expediting further dissolution of Mg.

$$Mg(OH)_2 + 2\,Cl^- \longrightarrow Mg^{2+} + 2\,Cl^- + 2\,OH^-$$

Magnesium alloys do not corrode uniformly, but exhibit a localized corrosion attack in aqueous environments. Because of the pitting corrosion mechanism and subsequent particle undermining, structural failure is difficult to predict.

B. In vitro corrosion testing

B.1 Experimental setup

The corrosion behaviour of the AZ31 alloy is characterized in static simulated body fluid. First, an experiment is designed to evaluate the corrosion rate over time. Taking into account the stoichiometry of the overall reaction, the amount of magnesium mass lost can be derived from the evolved volume of H_2, which is collected. The corrosion rate CR is then quantified at different points in time by means of (1).

$$CR = \frac{W}{A\,t\,\rho} \tag{1}$$

Here, CR is the corrosion rate, W the change in mass (g), A the original surface area exposed to the corrosive medium (cm^2), t the exposure (immersion) time (h) and ρ the mass density of the material (g/cm^3). Normalization with the density to express the CR as penetration rate is only meaningful for materials undergoing uniform corrosion.

A second experiment, combining a corrosion series with tensile testing, allows to determine the effect of material degradation on the mechanical properties.

A third experiment is performed in order to assess the effect of induced stresses on the corrosion attack.

B.2 Results

The stress-strain behaviour measured for different degrees of corrosion-induced mass loss is shown in Fig. 1. Both specimen strength and strain at fracture are seen to decrease significantly, even for moderate corrosion mass losses.

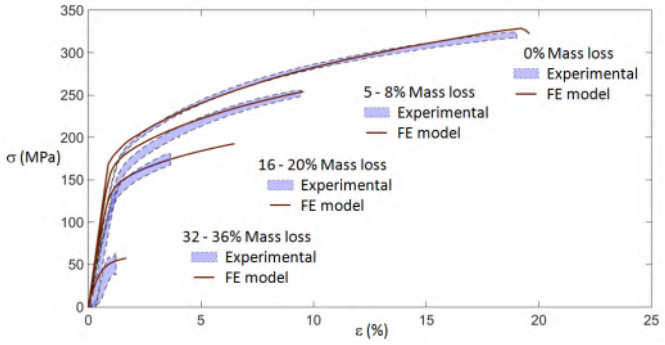

Fig. 1. True stress-strain curves for different degrees of mass loss: Experimental measurements versus FE simulation predictions

III. Corrosion model for magnesium stents

A. Methods

The damage model is implemented through a Fortran user subroutine or UMAT compatible with the finite element solver Abaqus/Standard (Dassault Systèmes, USA). This interface allows to define constitutive relationships of arbitrary complexity in addition to the material models already implemented in the Abaqus material library. Meshed generic stent geometries are readily created by means of the Python based open-source software pyFormex (bioMMeda, Ghent University). Finite element simulations are run on a high performance Linux computing cluster (184 CPU's) dedicated to computational mechanics.

B. Model development

The developed numerical framework [3], based on previous work by Wu et al. [4–6] and Grogan et al. [7] implements both pitting and stress corrosion. Provided material-specific calibration, this model is able to reproduce the effects of corrosive degradation on the mechanical properties, as well as the influence of residual stresses on the local corrosion rate. An element-specific scalar damage parameter d is introduced, representing the extent of corrosion-induced damage. A value of 0 corresponds to intact material. Once the damage parameter reaches its maximal value $d = 1$, the material is completely corroded and the corresponding element is effectively removed from the FE mesh, simulating mass loss due to corrosive degradation. *

Magnesium corrosion is assumed to be a superposition of two types of non-uniform corrosion processes: stochastic pitting corrosion (d_p) and stress-driven corrosion (d_{sc}):

$$d = (1 - f)\, d_p + f\, d_{sc} \tag{2}$$

where $f = 0.5$ for convenience.

The damage evolution laws (3) - (5) describe the assumed evolution of the corrosion damage parameters in surface elements. λ_p is an element-specific dimensionless pitting parameter for which random values are assigned initially. K_u (h^{-1}) is a kinetic parameter for the corrosion process representing the uniform degradation rate, δ_u, δ_{sc} (mm) and L_e (mm) are material and FE model characteristic lengths respectively and σ_{eq} (MPa) represents a measure for the internal stress driving the stress corrosion process, e.g. the maximum principal stress. S ($mm^2 h^{-0.5} N^{-1}$) and R (-) are constants related to the kinetics of the stress corrosion process depending on the corrosive environment. It is clear from equations (4) and (5) that stress corrosion only occurs when the equivalent stress σ_{eq} exceeds the value σ_{th} (MPa) and becomes more important as the internal stresses rise due to deformation.

$$\frac{\partial d_p}{\partial t} = \frac{\delta_u}{L_e}\, K_u\, \lambda_p \tag{3}$$

$$\frac{\partial d_{sc}}{\partial t} = \frac{L_e}{\delta_{sc}} \left(\frac{S\, \sigma_{eq}}{1 - d_{sc}} \right)^R \tag{4}$$

if $\sigma_{eq} \geq \sigma_{th} > 0$

$$\frac{\partial d_{sc}}{\partial t} = 0 \tag{5}$$

if $\sigma_{eq} < \sigma_{th}$

A random number generator, based on the standard Weibull distribution with probability density function (PDF) f(x), is used to assign λ_p values to all elements on the initial exposed surface. The probability of the value of λ_p to be in the range [a, b] is given by:

$$P\,[a \leq \lambda_p \leq b] = \int_a^b f(x) dx \tag{6}$$

$$f(x) = \gamma\, x^{\gamma - 1}\, e^{-x^\gamma} \qquad x \geq 0,\ \gamma > 0 \tag{7}$$

γ is a dimensionless distribution shape factor characterizing the probability density function. Increasing values of γ result in a more symmetric and narrow range of λ_p values being assigned to surface elements, corresponding to a more homogeneous corrosion process. For the modeling of non-uniform or localized corrosion, λ_p values are assigned according to an asymmetric distribution with lower γ value.

When an element is effectively removed, the neighbouring elements become subject to corrosion and inherit the value of the pitting parameter (8). The dimensionless scaling parameter β controls pit growth acceleration.

$$\lambda_p' = \beta\, \lambda_p \tag{8}$$

The influence of the damage parameter on the stress state σ is given by (9), where $\bar{\sigma}$ represents the stress tensor in the undamaged material. In damaged elements, the stress corresponding to a given strain value reduces as more damage is induced, governed by the evolution of the damage parameter d.

$$\sigma = (1 - d)\, \bar{\sigma} \tag{9}$$

*Unlike Abaqus/Explicit, Abaqus/Standard does not allow for element removal. Instead, the mechanical properties of corroded elements are set to nearly zero, so that they do not longer contribute to the mechanics of the object.

C. Model calibration

C.1 Calibration strategy

In order to calibrate the corrosion model, material model parameters and degradation constants are tuned by fitting the FE simulation results to the collected experimental data. The first requirement is that the mass loss vs. time curve predicted by the model corresponds qualitatively to the trend observed experimentally. The condition of the evolution of mass loss in time having to match the course observed, allows to determine γ and β. Second, the simulated average corrosion rate should quantitatively match the experimental value, which enables to set a value on the uniform degradation rate parameter K_u for given values of γ and β. Third, the model should properly capture the measured decrease in specimen mechanical integrity.

C.2 Results

The corrosion model is able to reproduce the two phase linear mass loss trend as a function of time. Given the good fit between FE predictions and experimental data (Fig. 1), one can conclude that the numerical framework captures the effect of a specific degree of corrosion-induced damage on the mechanical properties of the material relatively well.

IV. Modeling biodegradable magnesium stent mechanics

The developed corrosion model is applied to the FE modeling of realistic stent mechanics. The deployment and subsequent degradation of a degradable metal stent are modeled (Fig. 2, 3). Eventually, the framework is used to predict the loss in radial strength for increasing degrees of material loss.

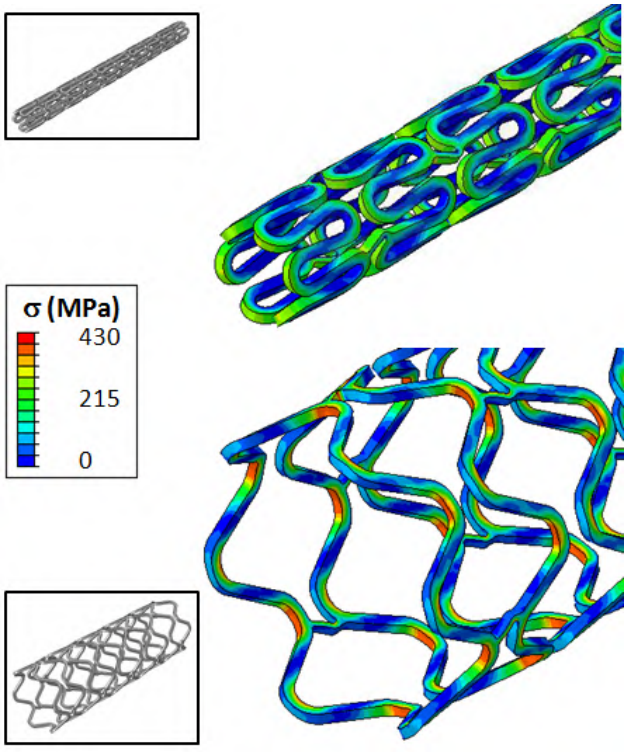

Fig. 2. FE simulation prediction for the stresses induced in the stent material upon deployment: Crimping (upper) and expansion (lower)

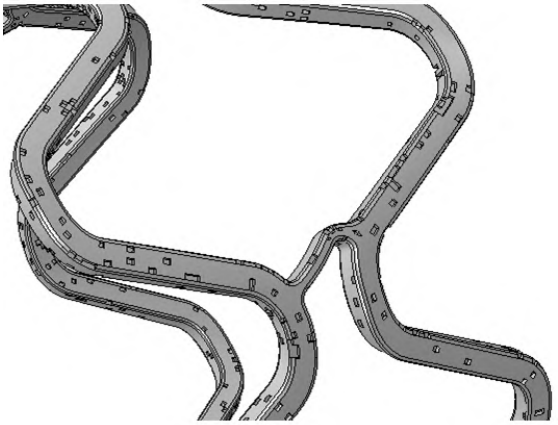

Fig. 3. FE simulation prediction for the pitting corrosion process (8.5% mass loss)

V. Conclusion and future work

An in vitro test system is designed with the aim of characterizing the corrosion behaviour of the AZ31 alloy in simulated body fluid. Quantitative data with regard to the dynamic corrosion rate and the effect of mass loss on the mechanical properties are collected. Considering the limited complexity of the in vitro test environment used, it cannot be expected to reproduce with great accuracy in vivo degradation processes. However, the efforts in this work clearly demonstrate the feasibility of using in vitro experimental data to calibrate a theoretical corrosion model dedicated to FE modeling of stent mechanics.

Since much of the inconsistency regarding the degradation characteristics of magnesium alloys stems from the choice of the test medium, adoption of new standards for in vitro studies is desirable, applying experimental conditions even more representative of the in vivo environment of endovascular devices.

In the future, the current corrosion modeling framework has to be made more robust, so that it becomes generally applicable. In particular, the time scaling in the evolution laws for different types of corrosion should be studied in more detail.

To prolonge the life time of the device, magnesium alloy stents are currently covered with a polymeric coating. New FE frameworks adopted to model the mechanics and degradation of these devices should implement realistic interaction between the substrate and coating.

References

[1] J. A. Ormiston and P. W. S. Serruys. Bioabsorbable coronary stents. *Circulation. Cardiovascular interventions*, 2(3):255–60, June 2009.

[2] R. Waksman, et al. Early- and long-term intravascular US and angiographic findings after bioabsorbable magnesium stent implantation in human coronary arteries. *JACC: Cardiovascular Interventions*, 2(4):312–20, 2009.

[3] N. Debusschere, et al. Modeling of coated biodegradable stents, Proceedings of the ASME 2012 Summer Bioengineering Conference, 2012.

[4] D. Gastaldi, et al. Continuum damage model for bioresorbable magnesium alloy devices - Application to coronary stents. *Journal of the mechanical behavior of biomedical materials*, 4(3):352–65, April 2011.

[5] W. Wu, et al. Finite element analyses for design evaluation of biodegradable magnesium alloy stents in arterial vessels. *Materials Science and Engineering: B*, 176(20):1733–1740, December 2011.

[6] W. Wu, et al. Experimental data confirm numerical modeling of the degradation process of magnesium alloys stents. *Acta biomaterialia*, 9(10):8730–9, November 2013.

[7] J. A. Grogan, et al. A corrosion model for bioabsorbable metallic stents. *Acta biomaterialia*, 7(9):3523–33, September 2011.

Contents

List of Figures

List of Tables

Chapter 1

Introduction

1.1 Coronary stenting

Coronary artery disease (CAD) is the number one cause of death in the Western world. Formation of atherosclerotic plaques (fatty deposits) leads to narrowing of the coronary arteries. Eventually the myocardium is cut off from oxygen supply, which manifests itself as an acute myocardial infarction. Studies showing a decreasing fatality rate clearly suggest therapeutic advancement [1,2]. The most commonly performed method of revascularization is angioplasty with stenting, also known as percutaneous coronary intervention (PCI), altough in patients with multiple areas of coronary artery stenosis open chest bypass surgery offers better results [3,4]. About 10% of CAD patients undergo coronary artery bypass graft (CABG) surgery, during which a portion of a healthy blood vessel is used to create a bypass for the blocked artery. The majority of patients with CAD is treated by means of percutaneous interventions, including percutaneous transluminal coronary angioplasty (PTCA) and coronary artery stenting (CAS). A balloon catheter is passed over a guide-wire into the affected arterial segments, followed by inflation of the balloon to dilate the narrowed vessel as illustrated in Fig. 1.1. Stents, small mesh-like tubes deployed to ensure the artery remains open, can be both balloon expandable and self-expanding. Such minimally invasive surgery techniques improve prognosis compared to traditional bypass surgery by reducing incision size drastically, leading to less scarring, lower risk of infection, shorter hospitalization (ca. 1 day compared to 5 days) and faster recovery (ca. 2 weeks compared to 2 months) [5].

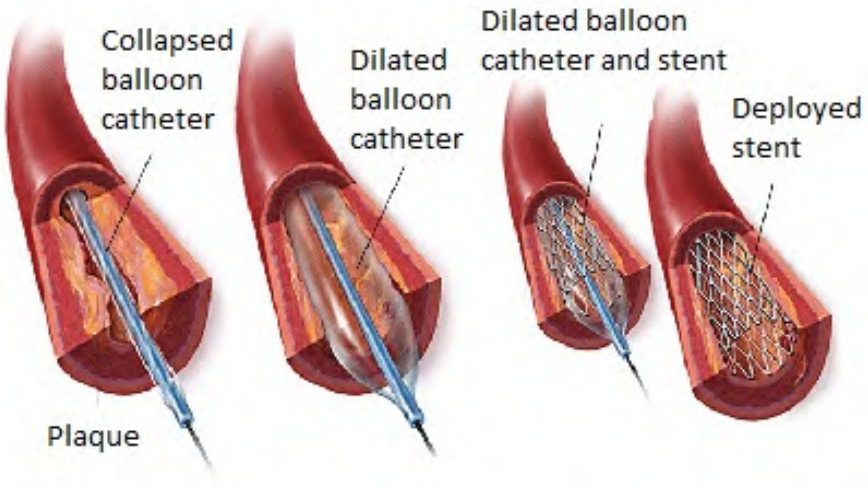

FIGURE 1.1: Angioplasty (left) and balloon expandable stenting (right) procedure [6]

1.2 Permanent versus biodegradable stents

Coronary artery stenting using permanent metal stents has been shown to reduce the rate of vessel recoil and restenosis compared to PTCA alone [7,8]. However, implantation of bare metal stents (BMS's) is still associated with thrombosis and in-stent restenosis, as well as delayed re-endothelialization and chronic inflammatory reactions [9, 10]. Thrombosis or blood clot formation is caused by activation of platelets in the vicinity of exposed metal surfaces [11]. Restenosis is due to a process called neointimal hyperplasia, referring to proliferation and migration of vascular smooth muscle cells induced by damage to the arterial wall [12]. The incidence of in-stent restenosis has been reduced significantly by the introduction of drug eluting stents (DES's) [4, 13]. A DES is coated with a polymer layer containing anti-proliferative drugs such as Sirolimus, Paclitaxel and Tacrolimus analogues. Controlled local release of these drugs inhibits neointimal hyperplasia pathways during a period up to four months after stent implantation [14]. Average coronary restenosis rates for a 6-month period post PCI are summarized in Table 1.1. Even for DES's late stent thrombosis remains a major concern, because of poor endothelialization of stent struts [15]. As a consequence prolonged antiplatelet therapy is required.

Type of intervention	Restenosis rate (%)	Source
Balloon dilation (PTCA)	50	[4]
Stenting BMS (PTCA + CAS)	20-30	[16]
Stenting DES (PTCA + CAS)	<10	[17]

TABLE 1.1: Restenosis rates at six months post PCI

Fully biodegradable coronary stents are being considered vigorously for over two decades, because they show considerable promise with regard to alleviating some of the long-term complications resulting from the presence of permanent stents. Biodegradable stents should be resorbed entirely by the body, retaining sufficient mechanical integrity during the process of degradation to allow the diseased blood vessel to heal (Fig. 1.2). This corresponds to a period of 6 to 12 months [18]. After the stent has disappeared, the vessel lumen maintains its diameter due to vascular remodeling. Furthermore, the selected material should degrade into nontoxic byproducts and invoke a minimal degree of inflammation (biocompatibility). Ideally, the corrosion products are readily soluble in the human body. A stent that is fully bioresorbable is unlikely to cause thrombogenic effects or in-stent restenosis. Also, such devices do not form an obstacle for possible future interventions. Biodegradable polymeric stents have potential as drug or gene delivery systems. Polymers widely explored for use in endovascular devices such as poly-L-lactic acid (PLLA), polyglycolic acid (PGA) and polycaprolactone (PCL) have a degradation time between 6 and 24 months. Polymers can be tailored to exhibit a well-defined degradational behaviour. Resorbable metals show the advantage of having mechanical properties closer to permanent metal alloys (section 2.1), but the degradation process is less predictable [19–24]. No stent material currently investigated combines all of the above properties, but magnesium alloys show great promise as materials for the (coronary) stent of the future. In particular, biocorrodible metal stents coated with a degradable polymer are expected to combine the benefits of both material classes.

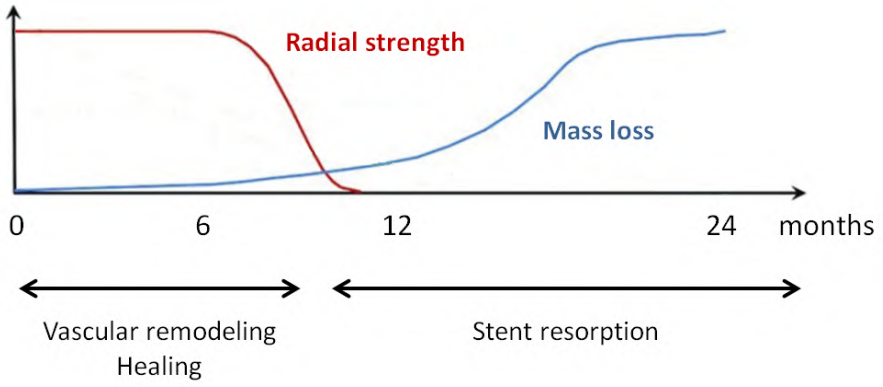

FIGURE 1.2: Biodegradable stent devices should maintain sufficient mechanical integrity to allow for healing and remodeling of the diseased artery. Eventually the stent is resorbed completely.

Clinical trial outcomes suggest sufficient long-term safety of fully biodegradable polymer stents, with acceptable stent recoil and reduced late stent thrombosis [25, 26]. Early clinical results for magnesium stents raise serious concerns with respect to safety. The first absorbable metallic stent implanted in human coronary arteries is the absorbable metal stent (AMS-1) developed by Biotronik [27]. Fast degradation and subsequent early loss of radial strength resulted in early recoil and neointima formation, causing a high

restenosis recurrence rate after 4 months (Fig. 1.3) [28]. Newer designs aim at prolonging the radial support to the diseased artery by changing the geometry, alloy composition, strut dimensions and by applying a polymer coating containing antiproliferative drugs. Although the first generation of the drug eluting absorbable metal scaffold (DREAMS) improved mechanical properties and reduced late lumen loss, the performance does not yet approach the one of currently available drug eluting polymer stents [29]. No cases of stent thrombosis have been reported [30]. The second generation DREAMS is currently being evaluated in the BIOSOLVE II trial.

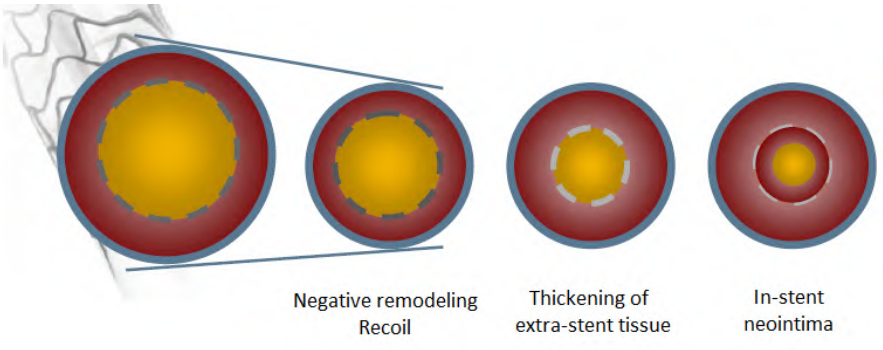

FIGURE 1.3: Contributions to lumen loss post implantation (adapted from [31])

AMS devices implanted in the pulmonary artery of a preterm baby [32] and the aorta of a newborn [33] were well tolerated. Absorbable stents are particularly preferable in infants and children because of their long life expectancy and growth. No adverse clinical effects were observed when AMS devices were implanted peripherally in order to treat critical lower limb ischemia [34–36].

1.3 Objectives

A finite element corrosion modeling framework was developed in order to predict absorbable metal stent mechanics. As the phenomenological model is material-specific, calibration is required. The aim of the work reported in this thesis is to design in vitro test protocols in order to characterize the corrosion behaviour of a typical magnesium alloy. More specifically, the corrosion rate and reduction in mechanical integrity over time are measured by means of immersion testing and tensile testing of thin foil specimens. These experimental data are used to calibrate the proposed corrosion model. Eventually, this framework is applied to simulate the deployment and degradation of a realistic magnesium stent geometry.

Chapter 2

Biodegradable metal stents

2.1 Biodegradable metals

The materials most often used to manufacture biodegradable metallic stents are magnesium (Mg) alloys and pure iron (Fe). Both metals are naturally present in the human body. As a consequence, they are broken down and resorbed completely when implanted, with little associated inflammatory response [10, 37, 38]. It is also important to assess possible cytotoxicity of products released into the human body upon degradation. While a high local Fe ion concentration may have a detrimental effect on endothelial cells [39], an in vitro study conducted by Sternberg et al. [40] suggests that elevated Mg levels keep in check smooth muscle cell proliferation and stimulate endothelial cell proliferation. These effects are expected to suppress neointimal thickening on the one hand and promote re-endothelialization of the foreign stent struts on the other hand. A study by Zhang et al. [41] showed an acceptable hemolysis (lower than 5% according to ISO 10993-4) and cell adhesion rate for the investigated Mg-Al-Zn alloy.

There are a number of considerations that have to be made when selecting a metal alloy for a biodegradable stent. The alloy has to exhibit sufficient strength and stiffness to avoid potential immediate recoil of the stent upon deployment. In general, biodegradable materials have mechanical properties inferior to those of traditional corrosion-resistant alloys used for balloon-expandable stents, such as stainless steel grade 316L. Iron stents however, exhibit good radial strength because of a high elastic modulus, limiting somewhat the required strut thickness. Magnesium alloys typically have a low elastic modulus. For magnesium and iron stents to match the performance of CoCr devices in terms of radial strength and recoil, Grogan et al. [42] reported an increase in the required strut cross-sectional area with a factor of 2.4 and 1.5 respectively. The lower ductility of magnesium alloys also complicates stent production and leads to a higher risk

of fracture [42, 43]. Tuning of the mechanical properties through alloying and specific pre-processing is required [44]. Table 2.1 summarizes relevant mechanical properties such as the Young's modulus E, yield strength σ_0 and average degradation rate CR for both corrosion-resistant and biodegradable stent alloys. Technically, the use of reduction in thickness to quantify the corrosion rate using units of mm/year is only suitable for metals undergoing uniform corrosion. As discussed in section 2.3, degradation of magnesium alloys in body fluid is characterised by non-uniform localized attack. The rate of degradation is cited in units of mm per year for the sake of comparison of the corrosion susceptibility for different alloys.

Alloy	E (GPa)	σ_0 (MPa)	$CR_{\ In\ vitro}$ (mm year^{-1})	Source
Stainless steel, grade 316L	193	380	-	[45]
Cobalt Chromium L605	243	629	-	[46]
Platinum chromium	203	480	-	[47]
Magnesium alloy WE43	45	216	1.35	[9, 48]
Magnesium alloy AZ31	44	138	1.02	[49, 50]
Magnesium alloy JDBM	45	293	0.28	[50, 51]
Iron, annealed	210	150	0.19	[52, 53]

TABLE 2.1: Mechanical and degradation properties of stent metal alloys (Young's modulus E, yield strength σ_0, average degradation rate $CR_{\ In\ vitro}$)

The change in mechanical properties directly depends on the rate of degradation. In a physiological environment, iron stents have been shown to degrade slowly, whereas the degradation of magnesium alloy stents occurs too fast to provide sufficient mechanical support during the process of arterial remodeling. Complete decomposition can be expected after 3 months [54]. The rate at which metallic materials corrode can be controlled by tuning of the alloy composition to benefit from solid solution strengthening and precipitation strengthening, and preprocessing (e.g. the effect of grain size [55–57] or surface modification treatment [58–60]). Addition of passivation agents such as chromium and nickel enhances the corrosion resistance of stainless steel alloys significantly. Aluminium and rare earth metals are added to magnesium based biomedical alloys to improve the mechanical strength and to slow down degradation [61, 62]. The addition of zinc also increases corrosion resistance [41,63,64]. The approximate composition of both corrosion-resistant and biodegradable stent alloys is given in Table 2.2. The corrosion mechanics of magnesium alloys are discussed in more detail in section 2.3. To date, the biggest challenge in the design of biodegradable metallic stents is to achieve appropriate mechanical stability, without compromising biocompatibility, as increased local concentrations of released metal species could interfere with biological processes [9, 37, 65, 66].

	Weigth percentage (%)												
Alloy	Fe	Cr	Ni	Mo	Co	W	Pt	Mg	Al	Zn	Zr	RE	Source
Stainless steel, 316L	>61	17	12	2.5									[52]
Cobalt Chromium L605	3	20	10		>50	15							[67]
Platinum Chromium	>35	18	9	2.6			33						[47]
Mg alloy WE43								>90				7	[48]
Mg alloy AZ31								96	3	1			[68]
Mg alloy JDBM	0.003		0.001					96.3		0.2	0.49	2.98	[50]
Iron, annealed	>99.5												[52]

TABLE 2.2: Composition (main constituents) of stent metal alloys
(RE: Rare earth metals a.o. Y, Nd and Gd)

2.2 Corrosive degradation

Metals undergo electrochemical oxidation in aggressive environments, whereas degradation of polymers is associated with disintegration and loss of macromolecular chain length. In a redox reaction an oxidizing agent, e.g. O_2 or H^+, removes electrons from a reducing agent. Metals readily give away electrons and are therefore oxidized according to the general oxidation half-reaction:

$$\mathrm{M} \longrightarrow \mathrm{M}^{n+} + \mathrm{n\ e}^{-}$$

For the transfer of electrons to be possible, the oxidants and reductants have to be in electrical contact, e.g. in an aqueous environment. In a physiological fluid, containing several inorganic ion species, the released metal ions typically combine to produce oxides or salts. The susceptibility to corrosion of a metal or alloy is reflected by its standard hydrogen electrode potential or alternatively by a potential measure more representative of the environment of application. Fig. 2.1 shows the galvanic series in flowing seawater, clearly illustrating the relative corrosion tendencies of engineering alloys. The more positive the electrode potential (anodic index), the more noble the material. Whenever two metals with differing electrode potentials are in electrical contact, galvanic corrosion occurs, i.e. the more active material or anode corrodes preferentially (acceleration), while corrosion of the more noble material is slowed down. Pure magnesium and magnesium alloys are the most active of all structural materials. Without modifications these materials have a low corrosion resistance and act as a sacrificial anode when coupled to other metals.

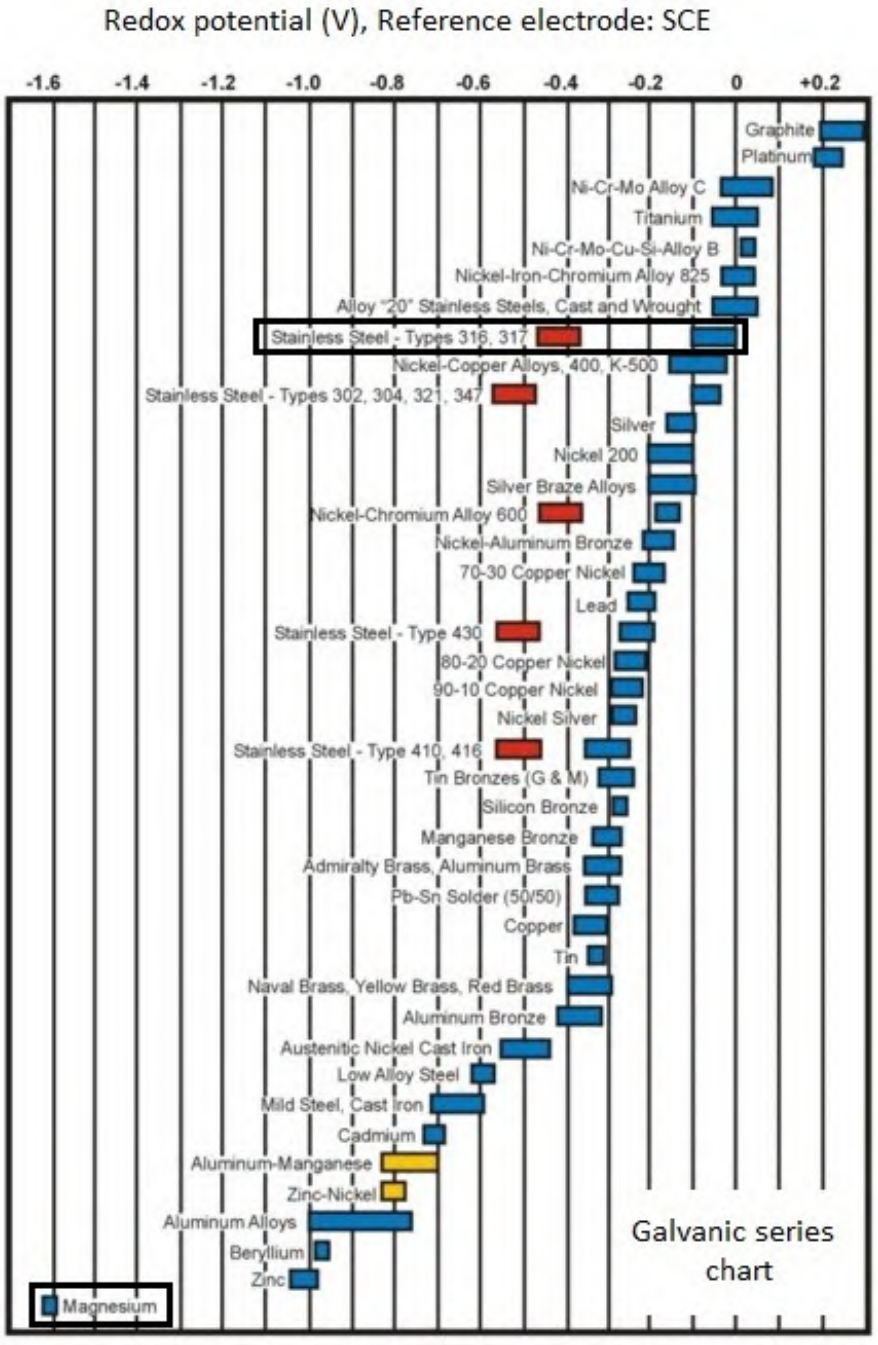

FIGURE 2.1: Galvanic series chart illustrating electrode potentials for engineering metal alloys relative to a saturated calomel electrode (SCE) in flowing seawater (adapted from [69])

2.3 Experimental characterisation of magnesium corrosion

It is generally accepted that stent dissolution should not occur before six months in order to prevent early mechanical device failure or fragment embolisation of the treated vessel. With regard to resorbable metallic endovascular devices, many studies have aimed to

improve the understanding and to determine quantitatively the rate of the degradation process in vivo. A major limitation of in vivo studies is that in vivo degradation rates cannot be assessed without disrupting the environment [37, 54]. The only possibility is the analysis of explanted specimens, which provides little information about ongoing processes. In vitro studies allow for the characterisation of the corrosion behaviour in aqueous or simulated physiological environment of pure magnesium and Mg alloys with more flexibility and nearly real-time [70–73]. However, some studies have shown significant discrepancy between the corrosion rate in vivo and the rate observed under simulated in vitro conditions which was substantially higher [74–76]. Witte et al. [75] reported in vitro corrosion rates four orders of magnitude higher than corresponding in vivo results. Furthermore, the relative degradation susceptibility of two different Mg alloys was not predicted correctly based on standard in vitro experiments. Because of strongly simplifying test bench conditions, conclusions drawn from in vitro corrosion tests have not proven suitable to predict corrosion rates in vivo, where numerous factors contribute to a very complex dynamic environment. This section reviews important experimental aspects with respect to the design of an appropriate in vitro environment for corrosion testing of magnesium and its alloys.

2.3.1 Corrosive degradation mechanism

Corrosion attack can occur on the different material phases present in a magnesium alloy. Since the main constituent Mg is very reactive in aqeous environment, its corrosion properties dictate those of the alloy. The understanding of corrosion of pure magnesium in aqueous environments provides the basis to investigate corrosion of alloys. Pure magnesium corrosion proceeds by an electrochemical reaction with water producing magnesium hydroxide and hydrogen gas. For each magnesium atom that is dissolved, one molecule of H_2 is produced.

$$2\ Mg + 2\ H^+ + 2\ H_2O \longrightarrow 2\ Mg^{2+} + 2\ OH^- + 2\ H_2 \quad \text{(Overall reaction)}$$

$$Mg^{2+} + 2\ OH^- \longrightarrow Mg(OH)_2 \downarrow \quad \text{(Product formation)}$$

The overall corrosion reaction corresponds to the sum of the following partial reactions [70]:

$$2\ Mg \longrightarrow 2\ Mg^+ + 2\ e^- \quad \text{(Anodic reaction)}$$

$$2\ H^+ + 2\ e^- \longrightarrow H_2 \quad \text{(Cathodic reaction)}$$

$$2\ Mg^{+} + 2\ H_2O \longrightarrow 2\ Mg^{2+} + 2\ OH^{-} + H_2 \quad \text{(Chemical reaction)}$$

As the overall reaction consumes H^{+} and produces OH^{-}, the pH increases, favoring the formation of a $Mg(OH)_2$ film on the magnesium surface (precipitation reaction). The deposited semi-permeable layer acts as a protective barrier, slowing down further corrosion.

More recently, Atrens et al. [72] have proposed a more detailed mechanism, indicating Mg^{+} as an intermediate in the reaction sequence between metallic Mg and Mg^{2+}:

$$Mg \longrightarrow Mg^{+} + e^{-} \quad \text{(Anodic reaction)}$$

$$k\ Mg^{+} \longrightarrow k\ Mg^{2+} + k\ e^{-} \quad \text{(Anodic reaction)}$$

$$(1+k)\ H_2O + (1+k)\ e^{-} \longrightarrow 1/2\ (1+k)\ H_2 + (1+k)\ OH^{-} \quad \text{(Cathodic reaction)}$$

$$(1-k)\ Mg^{+} + (1-k)\ H_2O + (1-k)\ OH^{-} \longrightarrow (1-k)\ Mg(OH)_2 + 1/2\ (1-k)\ H_2$$
(Product formation)

In the anodic reactions, metallic Mg is converted to Mg^{2+} ions involving the uni-positive ion Mg^{+} as an intermediate. Only a fraction k of the Mg^{+} ions reacts electrochemically to form Mg^{2+}, the stable Mg ionic species in aqueous solution. The complement $1-k$ reacts chemically to produce magnesium hydroxide. As a consequence, the corrosion of Mg is only partially electrochemical and electrochemical measurements are expected to yield a corrosion rate lower than the actual value. The real corrosion rate can be determined by means of gravimetric techniques (mass loss) or hydrogen evolution (Section 2.3.4).

In chloride containing electrolytes, passivity is lost completely as magnesium hydroxide, which is metastable in water, is converted into highly soluable magnesium chloride. The partially protective $Mg(OH)_2$ layer is broken down, exposing the magnesium metal directly to the corrosive medium and expediting further dissolution of Mg.

$$Mg(OH)_2 + 2\ Cl^{-} \longrightarrow Mg^{2+} + 2\ Cl^{-} + 2\ OH^{-}$$

In aqueous electrolyte solutions, magnesium is characterized by a negative free-corrosion (E_{corr}) and pitting potential (E_p). The partially protective film is potential dependent. For potentials lower than the pitting potential or for short periods of immersion, there is nearly complete film coverage of the metal surface and anodic dissolution of Mg is low.

As the potential increases beyond E_p or for prolonged immersion, the surface film is broken down, causing an increase in the anodic reaction rate and hydrogen production. This phenomenon is called the negative-difference effect (NDE) [77]. Localized corrosion attack is associated with additional mass loss because of undermining and falling out of grains. Pit formation increases the total surface area where corrosion can occur. The corrosion mechanisms for magnesium in aqueous environments are illustrated in Fig. 2.2.

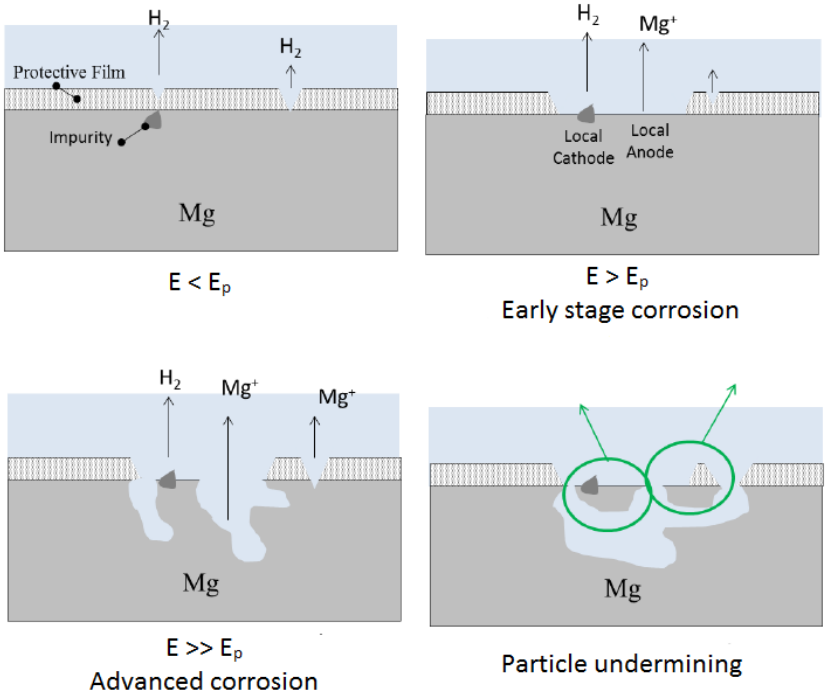

FIGURE 2.2: Schematic representation of the corrosion mechanisms for magnesium in aqueous environment (adapted from [78])

For magnesium alloys, the corrosion process is more complex than for pure magnesium. Metallurgical factors such as alloying additions influence the mechanism. Mg alloys show a higher resistance against corrosion attack. Formation of passivating Al_2O_3 hinders corrosion in aluminium containing alloys [63, 79–82]. Addition of Al to magnesium alloys has been shown to stabilize the protective film and increase corrosion resistance for an Al content of about 3 to maximally 4 wt.%. A higher Al content may lead to the presence of a second phase, which could be detrimental to the corrosion resistance as big second phase particles are undermined by corrosion fronts spreading laterally. Moreover, magnesium has the lowest standard potential of all engineering metals, meaning that it is readily subject to both macro- and microgalvanic corrosion when in electrical contact with other, more noble metals such as steel [80]. Song and Atrens [70] investigated the effect on corrosion resistance of increasing levels of alloying elements. Most metals serve as active cathodic sites when present at a level higher than an element specific tolerance limit, leading to micro-galvanic acceleration of magnesium corrosion. As Mg

is more reactive than the alloying metals which are concentrated at grain boundaries and impurities, the anode matrix close to these local cathodes has a corrosion potential lower than that of the second phase and is dissolved preferentially. A schematic of micro-galvanic corrosion is included in Fig. 2.3.

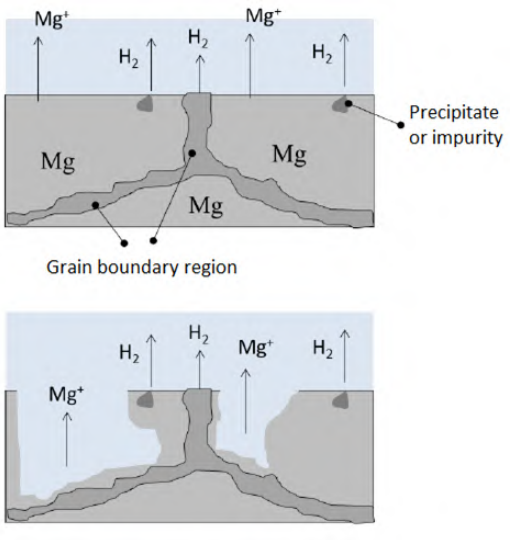

FIGURE 2.3: Schematic representation of micro-galvanic corrosion of magnesium alloys in aqueous environment (adapted from [78])

Scanning electron microscopy (SEM) studies confirm that localized pitting is the dominant corrosion mechanism for magnesium alloys such as the AZ31 alloy [57,83]. However, uniform corrosion would constitute the preferred mechanism of degradation, as it guarantees a more predictable device lifetime and longer retention of mechanical integrity, necessary to support the stented artery for a period of 6 to 12 months. The released particles should not have dimensions larger than a few microns to prevent them from occluding capillaries elsewhere in the vascular tree.

Magnesium alloys subject to static or cyclic loads in an aqueous environment are susceptible to stress corrosion cracking (SCC). Inter-granular SCC can be attributed to crack formation due to the preferential corrosion along grain boundaries, rich in the above mentioned secondary phases. Trans-granular SCC involves strain-induced rupture of the protective film and crack growth driven by hydrogen embrittlement [70]. These failure mechanisms are mainly being investigated in the context of structural alloys for load-bearing applications. Bobby Kannan et al. [84, 85] have reported about stress corrosion cracking in solution under different loading conditions. The relative importance of the second phase grain boundary and hydrogen embrittlement mechanisms was seen to depend on the type of magnesium alloy.

2.3.2 Immersion testing

2.3.2.1 Selection of suitable solutions for in vitro studies

Magnesium alloys degrade at a high rate in a saline environment. In order to evaluate the corrosion rate quantitatively, various in vitro test systems have been designed, applying different techniques. Electrochemical tests are a convenient way of characterizing corrosion properties based on measurements of the open circuit potential and polarization curves [72,83,86] or via electrochemical impedance spectroscopy [87] (Section 2.3.3). Immersion tests are also commonly used to study the corrosion of biodegradable metallic materials. Various (buffered) electrolyte solutions have been used to mimic the body fluid. The ionic compositions of natural human blood plasma, conventional simulated body fluid (c-SBF), revised simulated body fluid (r-SBF) and Hank's solution are given in Table 2.3. The composition of the immersion medium has a very important influence on the corrosion test results [88]. Zhen et al. [73] illustrate significant differences in corrosion potential and current density for different electrolyte systems. Besides inorganic ions (Na^+, Mg^{2+}, Ca^{2+}, Cl^-, HCO_3^-, HPO_4^{2-}), blood plasma and intercellular fluid also contain organic compounds (amino acids, proteins). Adsorption of proteins (e.g. albumin) and formation of biofilms on the surface of implants are difficult to quantify and mimic ex vivo. It has been shown that diffusion of metal ions is severly restricted in cell line biofilms, resulting in a more protective $Mg(OH)_2$ film [89–91], partly explaining the lower rate of degradation in vivo compared to approximating in vitro conditions. Specific studies confirm that the presence of proteins reduces the in vitro degradation rate [92–94]. The influence of aggresive ions present in physiological environment on the corrosion behaviour of biomedical Mg alloys is also widely investigated [83, 95–97]. For a chloride concentration exceeding 30 mmol/l, magnesium hydroxide is converted into highly soluable magnesium chloride $MgCl_2$ [98]. Body fluids have a chloride content above 100 mmol/l (Table 2.3), which explains the high corrosion rate observed for Mg alloys.

While a high Cl^- concentration accelerates the transformation of $Mg(OH)_2$ to $MgCl_2$ and promotes dissolution of the magnesium alloy, the associated release of OH^- ions results in an increase of the pH of the solution. The presence of Ca^{2+} in the medium is thought to promote the formation of a magnesium containing calcium phosphate surface layer [99,100], indicating that Ca^{2+} and HPO_4^{2-} ions take part in the surface reactions as well. High pH speeds up precipitation of these passive products [101].

$$x'\ Mg^{2+} + (x - x')\ Ca^{2+} + y\ PO_4^{3-} + z\ CO_3^{2-} + i\ OH^{1-} \longrightarrow\ (Mg, Ca)_x(PO_4)_y(CO_3)_z(OH)_i$$

Deposition of magnesium containing calcium phosphates and hydroxyapatites is also found in in vivo tests conducted to check the feasibility of biodegradable Mg alloys as materials for bone implants [102, 103]. The good biocompatibility and osteoconductivity of these products suggest that they would be beneficial for bone healing. Energy-dispersive X-ray spectroscopy (EDX) is often used to analyze the chemical composition of both surface layer and substrate. Alternative techniques to identify corrosion products formed on the surface of degraded specimens are X-ray crystallography (XRD) and fourier transform infrared spectroscopy (FTIR) [94, 100, 104]. The elemental composition of the corrosion product layers has been shown to depend strongly on the type of electrolyte solution [94].

Previously, aqueous NaCl solutions have often been used as electrolyte, but these media are not very representative of the in vivo conditions that endovascular devices are exposed to. Immersion tests in simple NaCl salt solutions result in a significant overestimation of the in vivo corrosion rate [89, 105]. As both inorganic ions and organic components appear to have a significant influence on the degradation process and rate of metal alloys, an electrolyte solution with similar components as human blood plasma should be selected to mimic the in vivo environment. The simulated body fluids summarized in Table 2.3 have ion concentrations very similar to plasma, but do not contain any organic components. Addition of proteins is expected to increase the complexity of the degradation mechanisms because of surface adsorption and to hinder the unequivocal interpretation of test results. When the Mg release into the immersion medium is to be analyzed, simplified phosphate buffered saline (PBS) solutions without Mg and Ca are often used (PBS^-).

	Ion concentration (mmol/l)			
Ion	c-SBF	r-SBF	Hank's	Human blood plasma
Na^+	142.0	142.0	141.6	142.0
K^+	5.0	5.0	5.37	5.0
Mg^{2+}	1.5	1.5	0.87	1.5
Ca^{2+}	2.5	2.5	1.26	2.5
Cl^-	147.8	103.0	144.62	103.0
HCO_3^-	4.2	27.0	4.17	27.0
HPO_4^{2-}	1.0	1.0	0.78	1.0
SO_4^{2-}	0.5	0.5	0.87	0.5
Source	[106]	[106]	[100]	[107]

TABLE 2.3: Ionic concentration of different artificial solutions compared to human blood plasma

The pH of the environment affects the stability of $Mg(OH)_2$ and consequently the rate of dissolution. Dissolution of magnesium has been shown to be lower at alkaline pH compared to neutral pH [95, 108]. Ng et al. [109] reported a decrease of 100% for the in vitro corrosion rate of magnesium for a change in pH from 7.4 to 8, clearly illustrating the importance of pH control in a pseudo-physiological test bench. Physiological solutions are often buffered at a pH-level close to the pH of human blood plasma equal to 7.25 [107].

2.3.2.2 In vitro test conditions

Yang and Zhang [100] found that the ratio of solution volume to sample surface area (V/S) significantly affected the biocorrosion behaviour of magnesium alloys in simulated body solutions. A low V/S ratio leads to higher pH, resisting further corrosion. For a V/S ratio above 6.7 ml/cm^2 this effect was found to be negligible. Selection of an appropriate V/S ratio appears to be necessary to simulate biodegradation of Mg alloy devices in different implantation environments, e.g. orthopaedic implants versus endovascular devices. If a spectroscopic technique is applied to evaluate the corrosion rate as described in section 2.3.4, the solution volume to sample surface area ratio cannot be too high in order to allow for detection of released Mg ions in the solution.

Another important factor determining the outcome of immersion tests is the flow rate of the solution. Indeed, the nature of the flow governs transport of reactants and products in the immersion medium, which in turn influences the surface reaction kinetics. Under static flow conditions corrosion of the test material may cease when an equilibrium concentration of ions is reached. In the body, dynamic flow conditions predominate due to blood flow and equilibrium is not achieved. To better simulate the blood flow inside the coronary arteries, dynamic immersion test benches have been designed [39, 104, 110, 111]. Lévesque et al. [104] noticed that the corrosion mechanism and rate vary with the applied shear stress. Diffusion of Mg ions away from and other ion species to the degrading material being the limiting factor for the corrosion surface reaction, flow and shear stress constitute important parameters. Furthermore, the type of formed products strongly depends on the composition of the corrosive medium. These observations demonstrate the need for a pseudo-physiological test bench, approximating the environmental conditions in arteries with an internal diameter between 1 and 6 mm, dedicated to the development of biodegradable metallic stents. A physiological solution is made to circulate within a polymethylmethacrylate (PMMA) channel. The dimensions of this channel are tuned to have fully developed laminar flow and to produce a sufficiently large zone of uniform shear stress. A dynamic range of shear stress and Reynolds number values, the two degrees of freedom in the system, is obtained by varying the flow speed and viscosity of the solution according to equation 2.1, where τ is the shear stress (Pa), μ the solution

viscosity (Pa s), Q the flux of the SBF solution (m^3/s) and W and H the width (m) and height (m) of the channel respectively. To ensure reproducible laminar flow conditions, the output of the centrifugal submersible pump is passed through a regulating valve and a compliance chamber (Fig. 2.4).

$$\tau = \frac{6\ \mu\ Q}{WH^2} \tag{2.1}$$

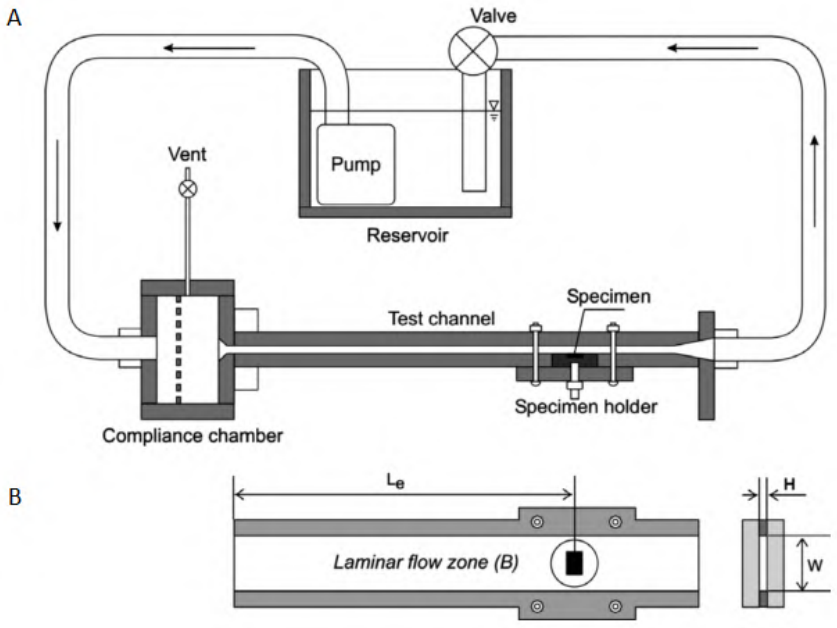

FIGURE 2.4: A, Schematic view of a dynamic test bench.
B, Close-up top view of the test channel with specimen in place (canal entrance length of laminar flow L_e, width W and height H of the test channel, adapted from [104])

Both static (with only gentle agitation in order to maintain homogeneous temperature and solute distribution throughout the solution) and dynamic tests have been performed using the setup from Fig. 2.4. During dynamic testing, the implant material is preferentially exposed to near-physiological shear stresses. Values for hemodynamic parameters representative of the flow in human coronary arteries are summarized in Table 2.4. Taking into account that shear stresses are typically higher in stenosed arteries than in healthy coronary arteries and that the presence of a deployed stent can lead to an extra 30% increase in shear stress, Lévesque et al. [104] adopted worst case values equal to 0.88 Pa (lower), 4.4 Pa (medium) and 8.8 Pa (upper, 10 times lower boundary).

	Re (-)	τ (Pa)	Source
Lower limit	75	0.33	[112–115]
Upper limit	250	1.24	[112–115]
Simulated lower	75	0.88	[104]
Simulated medium	75	4.4	[104]
Simulated upper	250	8.8	[104]

TABLE 2.4: Reynolds number (Re) and shear stress (τ) values representative of the flow conditions in coronary arteries

The AM60B-F alloy tested has been shown to degrade faster and more uniformly at low or moderate shear stress compared to static flow conditions, while highly localized corrosion is observed for high shear stress. Formation of a passive film is limiting the corrosion rate, but as the flow increases, local pH increase near the specimen surface is inhibited, thus promoting faster and more uniform degradation [116]. Other tests applying shakers (immersion) [117, 118] or rotating electrodes (electrochemical) [108] confirm that flow of the electrolyte solution accelerates the degradation process by reducing deposition of corrosion products.

Schille et al. [119, 120] incubated specimens of eight different Mg alloys in a modified Chandler-loop system using human whole blood and compared the results to static immersion tests in phosphate buffered saline (PBS). The release of Mg was 10 times higher in flowing blood than in static PBS. Moreover, the dynamic test protocol suggested an order of corrosion tendency different from static and electrochemical results [121], clearly establishing the issue concerning the reliability of conventional in vitro testing of material degradation in simulated body fluids. Apparently, relative corrosion tendencies of different alloys are strongly influenced by both the electrolyte composition and the test flow conditions. One of the reasons why static immersion tests are misleading in predicting the degradation characteristics of Mg alloys is the negative-difference effect (section 2.3.1).

Testing with human whole blood as opposed to a SBF raises the question of hemocompatibility. The influence of thrombogenicity on the degradation processes in vivo is largely unknown. Plasma proteins, such as fibrinogen, and platelets covering the surface may act as a barrier to diffusion and therefore slow down degradation or may enhance corrosion due to the formation of aeration cells (oxygen concentration giving rise to anodic and cathodic sites) at crevices between the substrate and the blood component layer [120]. Anticoagulation with heparin is necessary to prevent excessive blood clotting in the test bench, thus excluding the effect of thrombogenicity. Due to the limited stability of human whole blood, the tests were terminated after 6h, whereas simplified

immersion tests are often done over a time period of up to two weeks [61,93,94,122]. This experimental restriction limits the capabilities of this type of dynamic immersion tests to characterize the degradation behaviour in the long term, despite the more realistic medium (real blood) and flow conditions.

Finally, the mechanical loading of the specimen may also have an influence on the degradation process. Since immersion tests are mainly performed to study the corrosion mechanism and to evaluate the rate, specimens are mostly not subjected to any loads. Obviously, this is the case for stents deployed in a diseased coronary artery. Taking into account mechanical loading could be necessary to realistically simulate stress corrosion cracking and corrosion fatigue of a candidate stent material. Crack propagation is then driven by the combined effect of corrosive degradation and stress concentration.

2.3.3 Electrochemical testing

Corrosion occurs at a rate determined by the equilibrium between electrochemical reactions and the associated flow of electrons gives rise to an electrical current that can be measured. The potential of the metal balances the anodic and cathodic reactions. Therefore, electrochemical testing constitutes a standard method to characterize the corrosion behaviour of metals and their alloys. To this end, the metal to be studied is immersed in a representative electrolyte together with additional electrodes connected to a potentiostat. The potentiostat allows to manipulate the potential of the metal sample in a controlled manner and measure the resulting current (as a function of the potential). Usually, the first step is to measure the steady-state Open Circuit Potential (Eoc) or alternatively Corrosion Potential (Ecorr). Next, the sample can be polarized, meaning that the potential is forced away from the Eoc, while measuring the transient response current. The resulting polarization curves (Fig. 2.5) can be used to develop an electrical equivalent model for the corrosion process. A possible methodology to quantify the corrosion current (Icorr) and derive the corrosion rate is described in Section 2.3.4.

Another electrochemical testing technique is Electrochemical Impedance Spectroscopy (EIS). Here, the impedance of the system is measured over a range of frequencies. Again, the response is fitted to a circuit model in order to quantify polarization resistance and corrosion rate. The main advantage compared to other laboratory techniques is the possibility of using only very small amplitude signals that do not interfere with the phenomena being measured, e.g. a voltage between 5 and 50 mV.

2.3.4 Evaluation methodology of the corrosion rate

The most straightforward technique to quantify the corrosion rate (CR) is a gravimetric method. After removing adhered corrosion products from the test specimen, the mass loss due to corrosive degradation equals the initial mass minus the final mass. The corrosion rate is then readily expressed in units of mass loss per unit of surface area and per unit of time ($mg\ cm^{-2}\ h^{-1}$). The biggest disadvantage of gravimetric evaluation of the CR is the necessity to perturb the system and sacrifice the specimen when the desired time of immersion is reached. The largest error is introduced in the step of cleaning the test sample. Non of the strategies ensued to remove corrosion products from the surface are flawless: rinsing with distilled water [111] cannot remove deposited products completely, brushing [123] may leave scratches and therefore add to the mass loss, while aggresive chemicals such as chromic acid solutions [41, 99, 124] could react with the matrix if the washing time is too long. The corrosion rate can be expressed using the following equation:

$$CR = \frac{W}{A\ t\ \rho} \tag{2.2}$$

Here, CR is the corrosion rate, W the change in mass (g), A the original surface area exposed to the corrosive medium (cm^2), t the exposure (immersion) time (h) and ρ the mass density of the material (g/cm^3). Normalization with the density to express the CR as penetration rate is only meaningful for materials undergoing uniform corrosion.

Assessment of the corrosion rate by means of electrochemical methods is based on Faraday's law of electrolysis relating mass flux per unit area and time to electric current (equation 2.3). Since corrosion of magnesium alloys proceeds only partially electrochemical in aqueous solution (section 2.3.1), standard electrochemical methods cannot be applied to quantify the corrosion rate accurately. For electrolytic dissolution of a general species S, electric current is related to mass flow:

$$S \longrightarrow S^{z+} + z\ e^-$$

$$m = \frac{Q}{F}\ \frac{M}{z} \tag{2.3}$$

where m is the mass of material liberated (g), Q the total electric charge (C), F the Faraday constant (96 485 C/mol), M the molar mass (g/mol) and z the number of electrons transferred per ion.

Under the assumption of a constant current, the corrosion rate can be expressed as a function of corrosion current:

$$Q = I_{corr}\ t$$

$$CR = \frac{1}{F}\ \frac{M}{z}\ \frac{I_{corr}}{A} \tag{2.4}$$

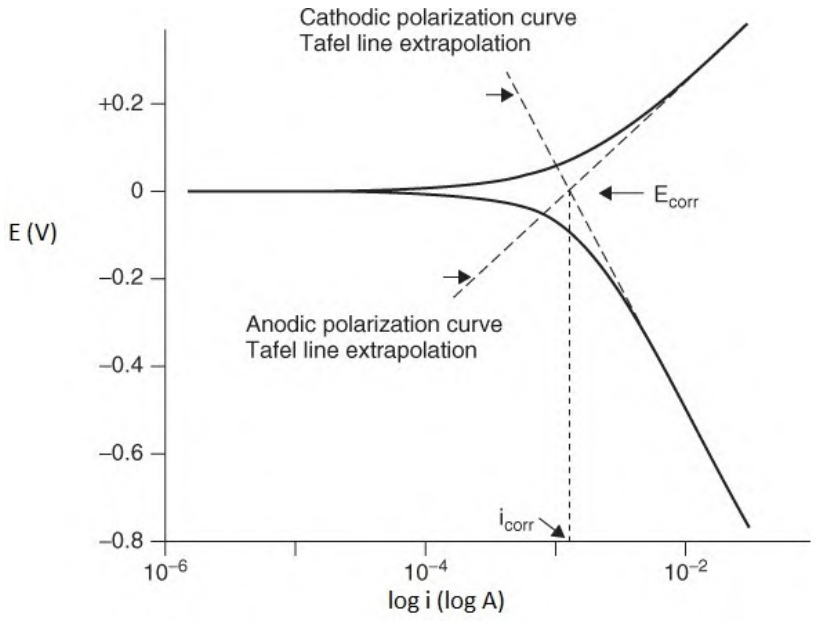

FIGURE 2.5: Tafel line extrapolation for determining electrochemical corrosion parameters (adapted from [125])

Classic Tafel analysis or Tafel line extrapolation is performed to find the anodic or cathodic current (i_{corr}) at their intersection by extrapolating the linear portions of a potential versus log current plot (Fig 2.5). As experimental data are in general not perfectly linear, curve fitting may be done to find the corrosion current, requiring knowledge of the corrosion kinetics. Other widely applied techniques applied are DC polarization resistance and AC impedance measurements [126]. All electrochemical techniques require a single anodic or cathodic reaction in order to yield a valid measure of the corrosion rate. Moreover, electrochemical testing applies accelerated corrosion, not representative of the material behaviour in vivo. Yfantis et al. [127] found electrochemical corrosion rates one order of magnitude higher than results from static immersion (mass loss) testing (Table 2.5). One can conclude that with respect to simulated physiological environments electrochemical tests are only useful to predict corrosion sequences of different materials and not for quantitative corrosion rate evaluation.

	CR ($mg\ cm^{-2}\ h^{-1}$)		
Material	Electrochemical test	Mass loss test	Source
Pure Mg	50.60	5.95	[127]
Mg AZ31	4.28	0.52	[127]
Pure Fe	$9.33\ 10^{-3}$	$1.07\ 10^{-3}$	[111]

TABLE 2.5: Comparison of corrosion rates determined by means of electrochemical and mass loss tests in 0.1 M NaCl

A particularly elegant method to measure the corrosion rate of magnesium alloys exposed to aqueous solutions is described by Song et al. [70]. An experimental setup like the one in Fig. 3.4 is used to collect the hydrogen gas produced by the corrosion reaction. The CR is derived from the volume of evolved hydrogen. The overall corrosion reaction indicates that dissolution of one atom of Mg generates one molecule of H_2. Therefore, evolution of one mole of H_2 corresponds to dissolution of one mole of Mg. As a consequence, measuring the volume of evolved hydrogen is equivalent to measuring the mass loss of the metal directly, i.e. after conversion to the appropriate units. To convert hydrogen evolution rates to mass loss rates based on the above assumption, the ideal gas law is used (equation 2.5).

$$p\ V = n\ R\ T \tag{2.5}$$

One can derive that at standard athmospheric pressure (p=101 325 Pa) and room temperature (T=293 K) 1 ml H_2 corresponds to 0.001 g Mg and subsequently calculate the CR by means of equation 2.2 (R=8.314 J/(mol K), $M_{Mg} = 24.305\ g/mol$).

The corrosion reaction considered is valid for pure magnesium metal. Yet, the proposed methodology remains applicable even for magnesium alloys with a single or multiphase microstructure. The α matrix phase in these alloys is a Mg-based solid solution, which is less corrosion resistant than secondary phases acting as cathodes. The magnesium in the α matrix can be assumed to dissolve according to the same reaction equation as the pure metal [79]. Particles falling out of the surface after being undermined by the corrosion process also contribute to the measured material loss, unless it constitutes a secondary phase that does not corrode and liberate H_2 within the same time scale. As all magnesium alloys of practical importance for biodegradable endovascular devices contain small amounts of alloying elements (less than 10%), the maximal error due to particle undermining is 10%.

Comparison of corrosion rates determined by means of mass loss measurement and hydrogen evolution shows good agreement between the two methods (Fig. 2.6). Furthermore, the H_2 evolution method is free from errors inherent to weight loss measurement procedures and allows monitoring of dynamic processes, as changes in the evolution rate of hydrogen directly reflect changes in corrosion rate.

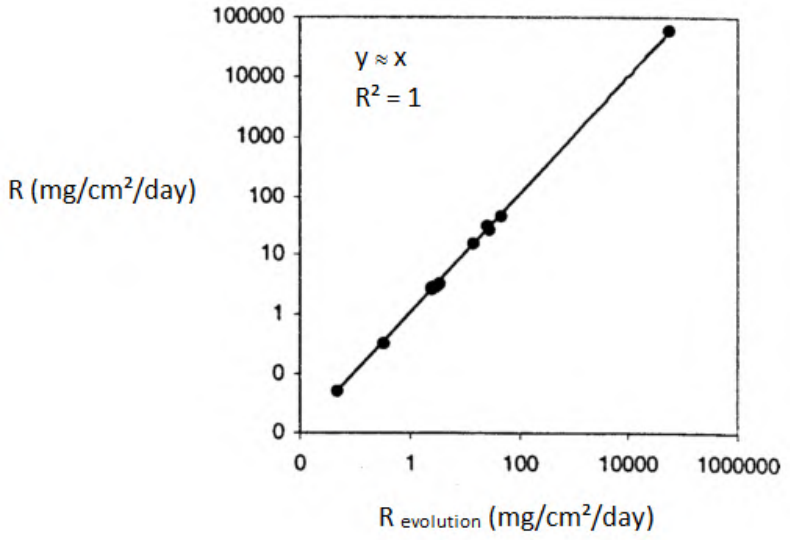

FIGURE 2.6: Correlation between the measured mass loss rate R for magnesium alloys and the mass loss rate derived from the hydrogen evolution rate $R_{evolution}$ (adapted from [128])

A prerequisite for using hydrogen evolution to estimate the corrosion rate of magnesium is that the contribution of oxygen reduction is negligible, as is the case in aggresive chloride containing solutions. In this study, oxygen reduction has been neglected in the corrosion mechanism (section 2.3.1).

One last strategy to measure the corrosion rate of metallic materials in vitro is by analyzing the concentration of ions released in the immersion solution. After the corrosion products have been dissolved in a strong acid (e.g. HNO_3), the concentrations of various ions are measured by means of inductively coupled plasma atomic emission spectroscopy (ICP-AES) or atomic absorption spectroscopy (AAS) [104, 111]. The corrosion rate is obtained from equation 2.6, with c and c_0 the instantaneous and initial released ion concentration (g/ml) respectively, V and V_0 the instantaneous and initial volume of solution (ml) respectively, A the original surface area exposed to the corrosive medium (cm^2) and t the exposure time (h). Similarly to the mass loss method, errors are introduced if the corrosion products cannot be completely removed into the solution.

$$CR = \frac{c\,V\ -\ c_0\,V_0}{A\,t} \tag{2.6}$$

2.3.5 Tuning degradation properties of candidate stent alloys

The main factor currently limiting the practical application of magnesium alloys in endovascular stent devices is the short degradation time. Stent struts typically have dimensions between 50 and 150 μm and the stents should maintain their mechanical integrity for at least 6 months. It is clear that the corrosion rate of Mg alloys currently investigated is too high. Although the material is covered by endothelial cells in vivo, resulting in slower degradation, the outcome of the localized corrosion process is difficult to predict, as opposed to uniformly corroding materials.

Several techniques have been adopted to improve the biodegradation properties of these materials. Novel, more durable Mg alloys are being designed by varying the amounts of several alloying elements. The gain in corrosion resistance that can be realized through alloying is limited due to the tolerance limits of solid solubility and the possible release of toxic or carcinogenic metal ions [129–131]. At very low levels, below the solubility limit, alloying elements generally retard anodic corrosion kinetics by incorporating in the α Mg matrix. For levels exceeding the solubility limit, which is fairly low in Mg based alloys, the addition of alloying elements leads to formation of second phase intermetallic particles acting as local cathodes. Such features in the microstructure promote micro-galvanic corrosion with an increased corrosion rate as a result. Also, some elements explored for alloying in structural applications, e.g. Mn, Ni, Ag, cannot be added to biomedical materials because of toxicity [130]. Recently, a novel Mg alloy (JDBM), containing relatively high amounts of zirconium and rare earth metals, emerged as a promising biomaterial [50, 51, 132]. Due to formation of a more compact and protective surface layer, this JDBM alloy exhibits a much lower degradation rate in vitro and a more uniform corrosion mechanism than more conventional Mg alloys, e.g. AZ31 and WE43 (Table 2.1). Such properties constitute huge advantages for application in biodegradable endovascular devices, because the time to structural failure is more predictable.

Degradable polymers can be used as a coating for Mg alloy stents and thus slow down the loss in mechanical properties of the Mg substrate. Such coatings also enable controlled drug release. Examples of suitable polymers are PLLA/PLGA [133–137] and PCL [136, 138]. Also calcium phosphate [117, 139, 140], titanium [141] and fluoride [142] coatings have been explored.

Changes in mechanical and biodegradation properties can also be introduced through different processing histories, e.g. extrusion and ageing heat treatment as opposed to casting [132], alkali-heat treatment [143,144] for surface modification or anodizing treatment to increase the thickness of the protective oxide film [64].

Decreased surface roughness appears to improve the passivation behaviour and reduce pitting tendency [145]. Fine grained Mg alloys have been shown to exhibit slightly better corrosion resistance because of a more homogeneous distribution of local anodes and cathodes [146,147]. In case particle undermining and eventual fallout constitute relevant mechanisms of degradation, less material is lost from a fine grained alloy compared to a coarse grained one, postponing mechanical failure.

2.4 Computational modeling of magnesium corrosion

In addition to in vitro and in vivo models designed to evaluate the performance of stent devices, advanced computational modeling can contribute to further optimization of stent design, mechanics and revascularization procedures. The main advantages of numerical modeling are its potential to perform parametric studies and the fact that virtual models are used instead of manufacturing large numbers of prototypes, reducing both cost and required time. Finite element models do not face most of the difficulties limiting the flexibility of in vitro models and can be designed to simulate highly realistic and complex conditions. Numerical modeling enables analysis of (medical) devices whose performance cannot be readily evaluated in vivo. Real life experiments are most often still required to calibrate the parameters in the computer model and validate the predictive capabilities. While numerical modeling of the mechanics of traditional non-degradable stents is a highly active field [42, 148–151], much less modeling approaches have been reported to account for degrading stent material. The current section reviews published methods to simulate corrosion of absorbable stent alloys. Table 2.6 briefly summarizes both the merits and limitations of corrosion modeling frameworks currently considered.

One numerical method applied to study the corrosion of metals is the boundary element method (BEM), discretizing only the domain boundaries of interest. This methodology has been applied successfully to the problem of galvanic corrosion of magnesium components coupled with other structural metal alloys [152–155]. Models implementing the BEM focus on predicting corrosion current densities for given potential fields, geometric factors (e.g. anode/cathode surface area ratio), electrolyte conditions and film thicknesses. Predicted current densities are readily related to mass loss rates. However, these studies don't take into account the movement of the corrosion surface. More recent numerical models employing the finite element method (FEM) and arbitrary Lagrangian Eulerian (ALE) meshing are capable of tracking a moving corrosion boundary [156–159]. The aim is to accurately predict the corrosion rate as well as the current-driven evolution of the corrosion surface arising from potential fields. Sun et al. [159] additionally account for time-dependent deposition of corrosion products at the interface and diffusion of reactants and products through the deposited layer. The approaches mentioned above are limited to fairly simple geometries and are used primarily for predictive modeling of localized corrosion, pit growth and galvanic corrosion interfaces. They have not proven suitable for incorporating corrosion in the modeling of the mechanical behaviour of complex three-dimensional structures such as absorbable metallic stents. Because of the difficulties in solving moving boundary problems, other modeling frameworks were explored.

A promising engineering approach to avoid the practical difficulties associated with developing physical corrosion models applicable to complex three-dimensional geometries is the use of continuum damage mechanics [160, 161]. Continuum damage theory allows to account for the effects of corrosion on the structural integrity without resorting to an explicit description of microscopic phenomena and their progression. The effects of progressing damage on the material mechanics are represented by means of arbitrary state variables. Furthermore, both a damage initiation criterion and a damage evolution law are required, e.g. a hardening function in plasticity formulations. Lemaitre and Desmorat [162] proposed to introduce a scalar damage parameter d and an effective stress $\bar{\sigma}_{ij}$ according to:

$$\bar{\sigma}_{ij} = \frac{\sigma_{ij}}{1-d} \tag{2.7}$$

Continuum damage mechanics has been applied to predict corrosion fatigue crack propagation or stress corrosion cracking (SCC) in structural materials under sustained loading in aggressive environment [163,164]. Wenman et al. [165] included the concept of initially assigning a random number between 0 and 1 to all finite elements indicating the local susceptibility to pitting and removing elements having reached a critical damage threshold. Both corrosion-induced pit formation and crack growth are simulated by means of FE deletion. In the next time increment of the FE routine the stresses are redistributed. Gastaldi et al. [166] have developed a phenomenological finite element framework dedicated to AMS modeling to reproduce the corrosion behaviour of magnesium alloys. In addition to uniform corrosion, stress mediated corrosion is implemented by means of a stress-dependent damage evolution law based on the work of da Costa-Mattos et al. [164]. The evolution of the free surface exposed to the aggressive environment is governed stochastically as proposed by Wenman et al. [165]. A good match was found between simulation and experimental results for two different magnesium alloy stent designs [167] (Fig. 2.7). The developed corrosion model has been applied in multiple numerical studies regarding optimization of AMS design, e.g. to achieve lower residual stresses in order to delay the loss of structural integrity [167–169].

The law governing the temporal evolution of the damage parameter is extended by Grogan et al. [49] through the introduction of an element-specific pitting parameter λ_e. The damage evolution law now accounts for heterogeneous or pitting corrosion. Numerically, the degree of heterogeneity of the corrosion process is described by the characteristics of the probability density function (PDF) of the distribution of the initial λ_e values. The narrower the range of λ_e values assigned to the elements, the more uniform the resulting corrosion process will be (Fig. 2.8). Once the damage parameter d reaches a value equal to 1, the corresponding element is removed from the FE mesh. Consequently

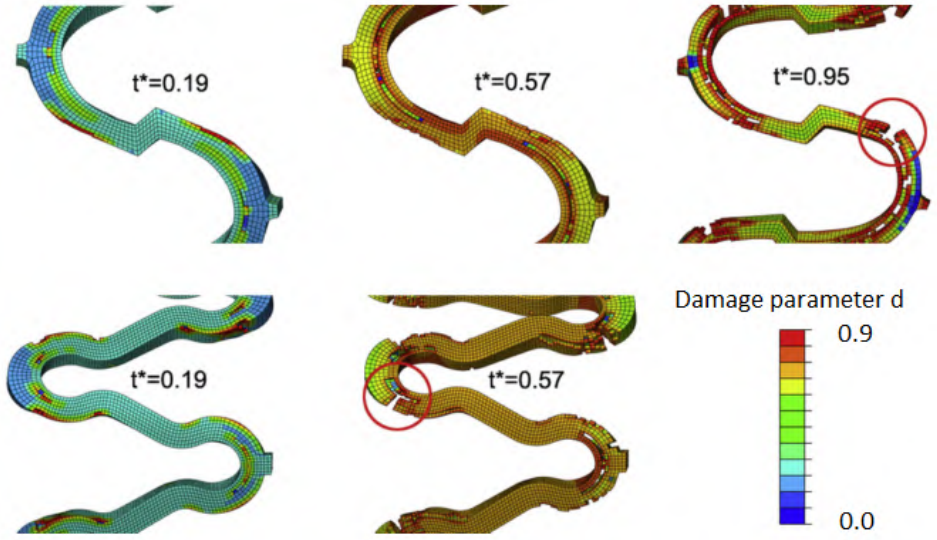

FIGURE 2.7: Predicted damage evolution in two magnesium alloy stent designs
Red circles highlight the locations on the stent rings with highest susceptibility to stress corrosion (normalized time unit t*, damage parameter d, adapted from [167])

the surface is updated based on an element connectivity map: Neighbouring elements become part of the surface and inherit the scaled pitting parameter value of the recently removed element. These steps correspond to the FE implementation of the corrosion surface evolution and controllable pit growth acceleration. Validation experiments have confirmed the capacity of the computational corrosion model to describe localized attack and subsequent reduction in mechanical integrity of Mg AZ31 foils, as well as the effects of mechanical loading on alloy corrosion. Due to the phenomenological nature, the developed model does not capture electrochemical processes, nor species evolution. As a consequence, the model predictions are specific to a given alloy, microstructure and medium. Recalibration is required when simulating corrosion of alloys with different composition and/or microstructure.

Based on previous work [49,166] Debusschere et al. [170] implemented constitutive equations in FE code to model both stress-driven and pitting corrosion of magnesium stent devices and checked the feasibility of accounting for the presence of a degradable coating. The considered coating comprised of the outer layer of finite elements. This approach allows to include the shielding of the underlying material, but not the specific mechanics and relative deformations of the coating-substrate couple.

As opposed to damage approaches, ALE corrosion models based on adaptive meshing do not rely on element removal and therefore are less sensitive to mesh resolution. The velocity at which surface facets move is explicitly controlled and can be calibrated based on experimental corrosion rates [171]. The current work addresses solving three-dimensional moving boundary problems, being the main limitation of adaptive meshing

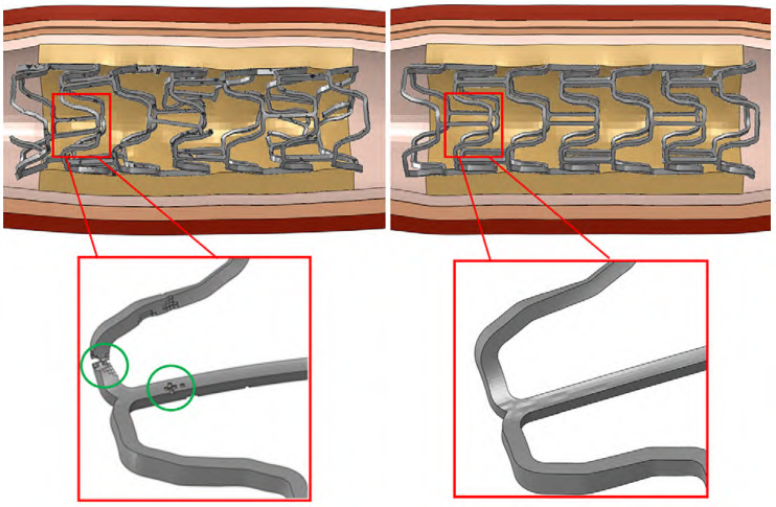

FIGURE 2.8: FE simulation results for predominantly pitting (left) and uniform (right) corrosion processes for an AMS deployed in an idealized artery model. Failure due to localized attack is expected to occur at the locations as circled (adapted from [49])

approaches. Grogan et al. [172] recently developed a physical corrosion model accounting for diffusion of magnesium ions. The evolution of the corrosion surface is governed by chemical and transport processes at the interface (Fig. 2.9). However, the assumption of diffusion control is only valid after the surface is covered by a corrosion product layer or alternatively a polymer coating or tissue layer. As the initial microgalvanic corrosion process at the bare surface cannot be considered to be diffusion controlled, tracking the boundary by means of adaptive meshing is very cumbersome. Long-term stent degradation, after formation of a corrosion product layer, is predicted correctly by the model described in [172]. Another methodology, extended to be suitable for three-dimensional geometries, is required to model the initial corrosion process by accounting for product deposition (adaptive remeshing) [159] or using level set functions without representing the interface explicitly, analogous to [173].

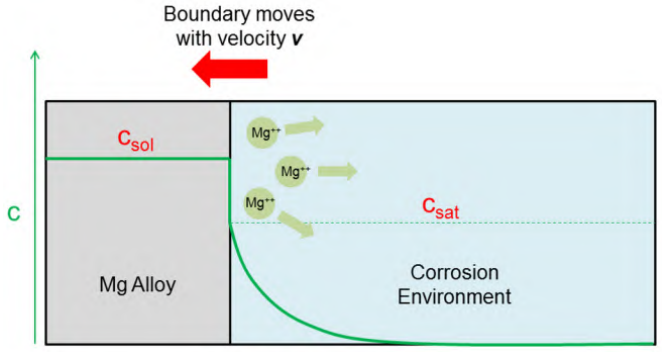

FIGURE 2.9: The velocity at which the corrosion front moves is governed by physical processes such as dissolution of Mg ions into the corrosive environment and diffusion away from the alloy surface (adapted from [172])

Research	Approach	Applicability	Modeling 3D AMS mechanics
Jia et al. [152] 2004	Boundary element method	Prediction of current densities for galvanic corrosion Two-dimensional, Electrical theory	-
Wenman et al. [165] 2008	Continuum damage mechanics	Prediction of pit/crack growth (SCC) and stress redistribution Two-dimensional, Mechanical control	-
Gastaldi et al. [166] 2011	Continuum damage mechanics	Simulation of stress-mediated corrosion Three-dimensional, Mechanical loading	X
Grogan et al. [49] 2011	Continuum damage mechanics	Simulation of pitting corrosion Three-dimensional	X
Debusschere et al. [170] 2012	Continuum damage mechanics	Simulation of stress-mediated and pitting corrosion Model formulation: Chapter 4	X
Sun et al. [159] 2012	Physical modeling ALE adaptive meshing	Tracking of a moving corrosion interface, while accounting for product deposition Two-dimensional, Mass transfer, Electrochemistry	-
Grogan et al. [172] 2014	Physical modeling ALE adaptive meshing	Simulation of long-term corrosion Three-dimensional, Diffusion control	X

TABLE 2.6: Chronological overview of corrosion modeling frameworks applicable to stent alloys

Chapter 3

Mechanical alloy characterisation

3.1 Materials and methods

3.1.1 Material

The Magnesium/Aluminium/Zinc alloy (AZ31, Mg 96/Al 3/Zn 1) to be tested is sourced in the form of a 0.25 mm thick foil (Goodfellow, UK). The foil has dimensions 100 x 100 x 0.25 mm and a net weight of 4.5 g (density $\rho = 1.8$ g/cm^3).

3.1.2 Specimen preparation

For the tests described in Section 3.2 specimens are cut from the 0.25 mm thick foil (Fig. 3.1). Square specimens with dimensions 10 x 10 mm are cut directly (experiment A). Dog bone and stent strut shaped specimens are created by means of lasercutting (experiment B and C).

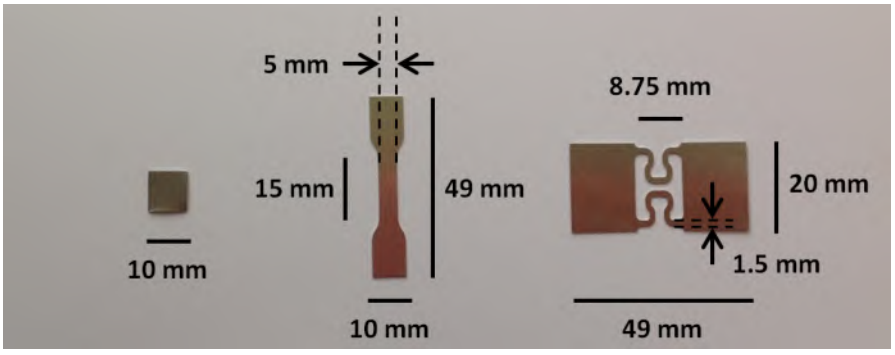

FIGURE 3.1: Photograph of the three types of experimental specimens used in experiments A, B and C with indication of dimensions (thickness 0.25 mm)

All samples are cleaned with isopropyl alcohol to remove oils from the surface and consequently dried in a glassware drying oven operating at 50 °C. In order to restrict corrosion to the gauge section of both the dog bone and stent cell shaped specimens, the end regions are covered with a layer of petroleum jelly. Petroleum jelly is an inexpensive water repellent and acts merely as a temporary protective coating. In order to remove corrosion products from magnesium alloys without attacking the base material a solution of 20% chromic acid (H_2CrO_3) in water is used. Next, the specimens are rinsed in ethanol and dried. Samples to be imaged by means of scanning electron microscopy are put in a vacuum furnace for 4 hours to remove possible contaminants. The presence of a vacuum prevents further oxidation of the magnesium metal.

3.1.3 Reference stent geometries

The stent strut geometry used in this work is similar to the Absorbable Metal Stent (AMS) developed by Biotronik. The stent geometry shown in Fig. 3.2 combines optimal flexibility for delivery and sufficient mechanical properties. The design also aims at reducing the risk of particles falling out as a consequence of localized corrosion and subsequent embolization [74]. Different absorbable magnesium stent designs recently used in clinical trials are shown in Fig. 3.3 and the main characteristics are summarized in Table 3.1.

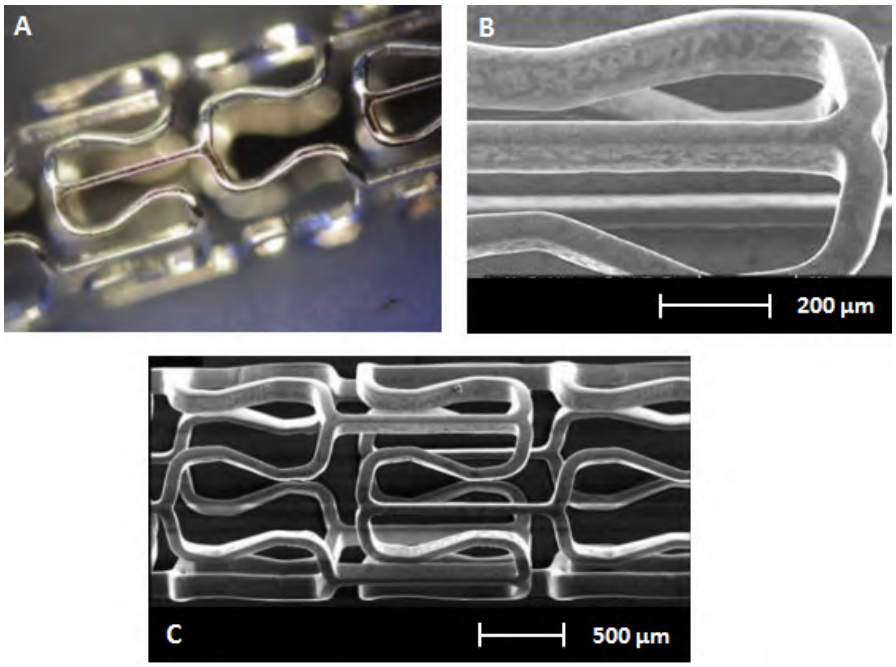

FIGURE 3.2: A, The absorbable metallic stent (AMS-1) by Biotronik, adapted from [174].
B, High magnification SEM image of the AMS-1 stent, adapted from [175].
C, Low magnification SEM image of the AMS-1 stent, adapted from [74].

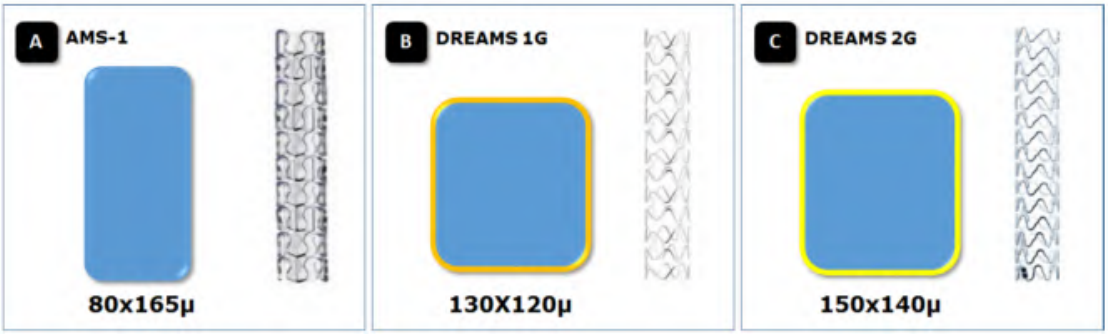

FIGURE 3.3: Cross-sectional profile and strut geometry of AMS-1 (A), DREAMS 1st generation (B) and DREAMS 2nd generation (C) [29].

	AMS-1	Magic (AMS-2)	DREAMS 1G	DREAMS 2G
Material	Mg WE43	Mg (Zr, Y, RE)	Mg (Zr, Y, RE)	Mg WE43
Strut dimensions (μm)	80x165	120x120	130x120	150x140
Coating	-	-	PLGA	PLLA
Coating thickness (μm)	-	-	1	7
Source	[18]	[10, 176]	[29, 177]	[29, 177]

TABLE 3.1: Characteristics of different absorbable magnesium stent designs (Biotronik) used in clinical trials

3.1.4 Simulated body fluid

The corrosive medium used for immersion testing is conventional simulated body fluid (c-SBF) (Table 2.3). c-SBF has ion concentrations equal to those of blood plasma, except for Cl^- and HCO_3^-. The main advantage compared to revised simulated body fluid (r-SBF) is a higher stability with respect to changes in ion concentration and pH upon storage [106]. The solution is prepared by dissolving the reagents in the sequence listed in Table 3.2 in distilled water (approximately 700 ml), while magnetically stirring and heating to 36.5 °C. Each reagent is added as soon as the preceding component is completely dissolved. Titration with 1M HCl aqueous solution is performed to adjust the pH to 7.4. After cooling to room temperature, pure water is added to adjust the volume to 1000 ml. Since the pH has an influence on the in vitro corrosion rate, the test solution is buffered using tris(hydroxylmethyl)aminomethane (TRIS). The electrolyte solution is eventually stored in a closed container at 4 °C for maximally 8 weeks.

Reagent	Amount for 1000 ml of c-SBF
NaCl	8.036 g
$NaHCO_3$	0.352 g
KCl	0.225 g
$K_2HPO_4 \cdot 3H_2O$	0.230 g
$MgCl_2 \cdot 6H_2O$	0.311 g
1M HCl	40 ml
$CaCl_2$	0.293 g
Na_2SO_4	0.072 g
TRIS	6.063 g
1M HCl	$\rightleftharpoons$ 0.2 ml

TABLE 3.2: Amounts of reagents for the preparation of 1000 ml of c-SBF, in the order of addition [106]

3.1.5 Tensile testing

Tensile testing is carried out on an Instron 5800R electromechanical testing system with a static 1 kN load cell. The speed of the crossheads is set to 2 mm/min in all tests. The analog signal coming from the system is sampled at a frequency of 10 Hz. A scale of 50 N/V and 0.5 mm/V are used to represent accurately the force and displacement range respectively. The data are read into a LabVIEW (National Instruments) based program and exported for analysis.

The engineering stress-strain curves measured experimentally do not give a true indication of the material deformation, because these measures are derived using only the initial dimensions of the specimen (Eq. 3.1). In tension the cross-sectional area decreases, causing the load required to continue deformation to fall off. As a result the engineering stress decreases beyond the point of maximal withstood load. In reality, a metal continues to strain-harden up to the point of fracture, which is captured by the true stress σ and strain ϵ based on the instantaneous length and cross-sectional area (Eq. 3.2).

$$\begin{aligned} s &= \frac{F}{A_0} \\ e &= \frac{\Delta L}{L_0} \end{aligned} \tag{3.1}$$

$$\begin{aligned} \sigma &= \frac{F}{A} \\ \epsilon &= \ln \frac{L}{L_0} \end{aligned} \tag{3.2}$$

True stress and strain are readily derived from the engineering measures s and e by means of equation 3.3. One condition is the homogeneous distribution of strain along the entire specimen gauge length.

$$\begin{aligned} \sigma &= s\ (e+1) \\ \epsilon &= \ln(e+1) \end{aligned} \tag{3.3}$$

3.2 Experimental setup

3.2.1 Determination of corrosion rate (A)

To measure the corrosion rate as a function of time, square Mg AZ31 specimens are immersed in simulated body fluid. The hydrogen gas produced by the corrosion reaction is collected by means of the setup illustrated in Fig. 3.4, including an upside down glass funnel and graduated test tube or buret. As H_2 gas bubbles up, it displaces an equivalent volume of physiological fluid from the buret. A thermostatically controlled oil bath is used to maintain the solution temperature at 36.5 °C. Distilled water is added to the container to compensate for fluid loss due to evaporation, which is approximately 10 ml per 24 hours. Dynamic measurement of the evolved H_2 volume at regular time intervals allows to quantify the in vitro corrosion rate without having to perturb the system.

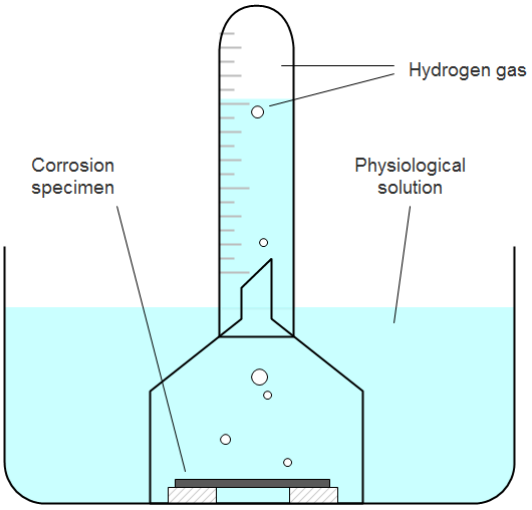

FIGURE 3.4: Experimental setup to collect H_2 produced by the corrosion reaction of Mg AZ31 alloy in simulated body fluid

An extra test is performed in order to investigate the effect on the corrosion rate of galvanic corrosion due to the simultaneous presence of magnesium and an other metal alloy in the electrolyte. This situation may occur when the corrosion testing is to be combined with simultaneous (tensile) loading of the specimen. The suitability of an

experiment requiring a magnesium alloy and another (less active) metal alloy to be in electrical contact is checked.

Scanning electron microscopy (SEM) is used to verify the corrosion mechanism based on the topology of the surface.

3.2.2 Effect of corrosion on mechanical properties (B)

In order to assess the effect of corrosive degradation on the mechanical properties of the AZ31 alloy, stress-strain curves are measured. Prior to tensile testing, dog bone specimens cut from a thin foil are immersed in simulated body fluid. The ratio of solution volume to exposed sample surface area (V/S) is approximately 50 ml/cm^2. Specimens are removed from the immersion medium at regular points in time: 1h, 3h, 6h, 24h, 48h, 72h and 96h. The corresponding mass loss is determined gravimetrically, which requires removal of corrosion products from the specimen gauge region surface by means of a chromic acid solution. The dog bone specimens are eventually loaded in uniaxial tension to fracture using a constant crosshead speed of 2 mm/min.

3.2.3 Influence of a tensile load on corrosion (C)

Stent strut shaped specimens (Fig. 3.1) are loaded in uniaxial tension in a controlled way and brought in corrosive environment afterwards. The degradation process of an unloaded specimen serves as a reference. The effect of deformation and the associated induced stresses on the local corrosion behaviour is assessed qualitatively.

3.3 Results and discussion

3.3.1 Determination of corrosion rate (A)

Initially a low corrosion rate of about 0.080 $mg\ cm^{-2}\ h^{-1}$ is observed (Fig. 4.8). After 6 hours of immersion the instantaneous corrosion rate increases significantly up to a value of 0.115 $mg\ cm^{-2}\ h^{-1}$. For this nearly steady rate of mass loss an average corrosion rate of 0.103 $mg\ cm^{-2}\ h^{-1}$ is evaluated. The pH of the solution is seen to increase slightly, from 7.4 up to a value of 7.8, over the course of the measurements (96 hours), which may have a decelerating effect on degradation. Therefore, the pH of the solution is measured regularly and if necessary adjusted to a constant value of 7.4.

The observations with respect to the instantaneous corrosion rate are not in agreement with the reports of other authors [99, 100]. The decrease in mass loss rate after about 6 hours of immersion reported is thought to occur due to formation of a partially protective $Mg(OH)_2$ layer on the alloy surface. For longer immersion times the corrosion rate remains fairly constant. This behaviour does correspond reasonably well to the results of similar static immersion testing by Grogan et al. [78] and the long-term average corrosion rate is of the same order of magnitude: 0.103 versus 0.084 $mg\ cm^{-2}\ h^{-1}$.

The AZ31 mass loss rate values for the in vitro test conditions used are one or two orders of magnitude higher than in vivo WE43 degradation rates measured for the novel DREAMS device [178]. This discrepancy can be explained by the relatively high Cl^- level in the electrolyte solution and the absence of proteins and cells. The in vitro environment was designed to mimic the in vivo situation as closely as possible, except for the exact in vivo flow conditions, which were not recreated in vitro, and the influence on the degradation process and transport phenomena by organic species such as proteins and cell lines. In particular, extremely long immersion times should not be considered as cell adhesion or endothelialization is expected to occur in vivo after a few days [74].

The corrosion rate of the AZ31 Mg alloy has proven to be too high, even for temporary scaffolding applications. Therefore, several strategies are considered to improve the corrosion resistance of such alloys (Section 2.3.5).

From the SEM images of the specimen surface, localized corrosion is seen to initiate with the formation of small irregular pits growing as a function of time (Fig. 3.5). After 6 hours of immersion in a corrosive medium, the pit diameter is between 50 and 100 μm. Cracks are observed in the surface of the material as well. It can be concluded that localized pitting corrosion constitutes the primary type of corrosion attack for the AZ31 magnesium alloy in physiological electrolyte solutions. The main disadvantage of pitting corrosion compared to uniform corrosion is the possibility of a significant reduction in mechanical strength, thus stent scaffolding support, even for a modest percentage of mass loss. This is a highly undesirable trait for the application of AMS.

Given the significant difference in redox potential or anodic index between magnesium and stainless steel alloys (Fig. 2.1), galvanic corrosion is expected to take place whenever these materials are in electrical contact (aqueous environment). Indeed, the magnesium mass loss rate is seen to increase by a factor of 1.3 compared to a situation where no galvanic corrosion occurs. As a consequence, the acceleration of mass loss due to galvanic corrosion would obscure any relevant measurements.

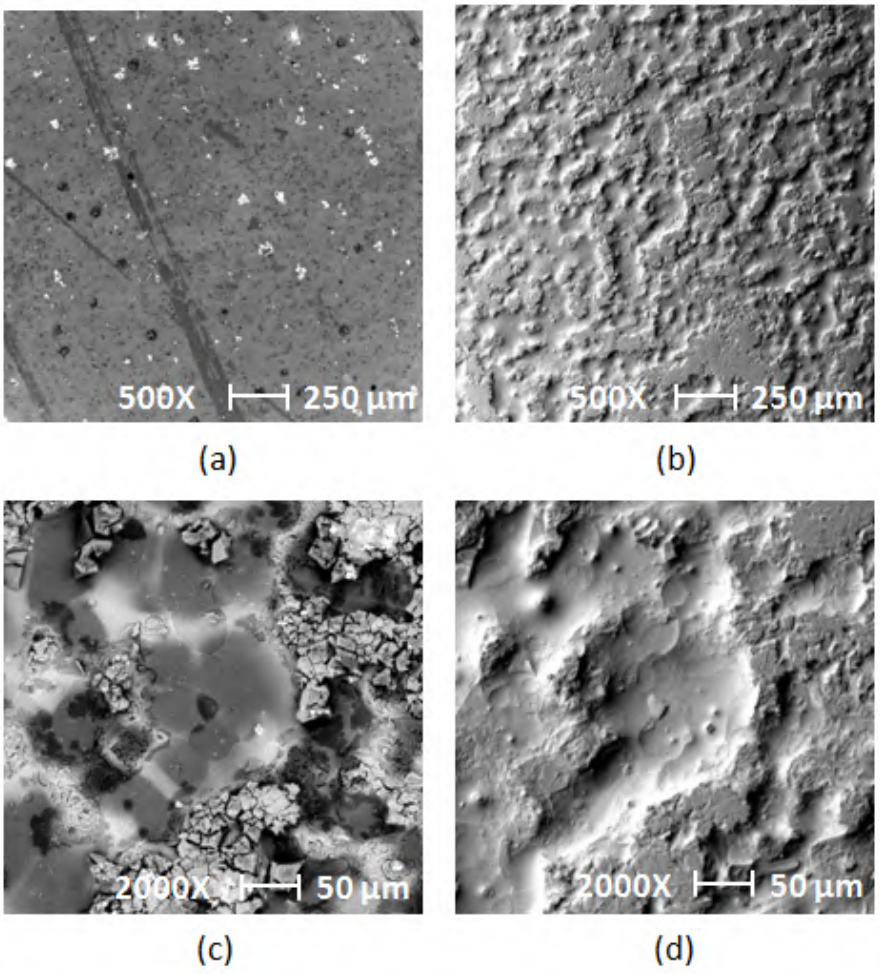

FIGURE 3.5: SEM images of the specimen corrosion surface
(a) Prior to immersion, (b) After 6 hours of immersion,
(c) Corrosion pit with visible precipitates, (d) Corrosion pit without precipitates

3.3.2 Effect of corrosion on mechanical properties (B)

The combination of the corrosion series described in Section 3.2.2 and tensile testing enables to quantify the effect of progressive corrosion damage on the mechanical integrity of the material. The resulting true stress-strain curves establishing the deformation characteristics of the AZ31 alloy are shown in Fig. 4.10. The reduction in specimen strength with corrosion mass loss is represented in another format in Fig. 4.11. The ultimate tensile strength (UTS), which is the engineering stress value for the maximal load withstood, is used to quantify the specimen strength.

Both specimen strength and strain at fracture are seen to decrease significantly, even for moderate corrosion mass losses. For small percentages of mass loss, up to 3%, the UTS decreases by 8% and the maximal strain by 43%. For relatively high percentages of mass loss, up to 20%, these measures fall of by 50% and 68% respectively.

3.3.3 Influence of a tensile load on corrosion (C)

When comparing the corrosion attack on unloaded and loaded struts, differences with regard to the degradation pattern are observed. However, the visual evidence is not at all conclusive and doesn't point out a significant acceleration of the corrosion process due to induced stresses in the material. Bobby Kannan et al. [84] reported significant stress corrosion susceptibilities for magnesium alloys similar to the AZ31 alloy studied in this work.

Chapter 4

Corrosion model for magnesium stents

4.1 Methods

The damage model is implemented through a Fortran user material subroutine or UMAT, compatible with the finite element solver Abaqus/Standard (Dassault Systèmes, USA). This interface allows to define constitutive relationships of arbitrary complexity in addition to the material models already implemented in the Abaqus material library. Meshed generic stent geometries are readily created by means of the Python based open-source software pyFormex (bioMMeda, Ghent University). Furthermore, this framework allows to write complete Abaqus input files. Finite element simulations are run on a high performance Linux computing cluster (184 CPU's) dedicated to computational mechanics.

4.2 Model development

Finite element modeling has become an indispensable tool for design and virtual testing of endovascular devices. The developed numerical framework [170], based on previous work by Wu et al. [166,167,169] and Grogan et al. [49], implements magnesium corrosion. Provided material-specific calibration (Section 4.3), this model is able to reproduce the effects of corrosive degradation on the mechanical properties, as well as the influence of residual stresses on the local corrosion rate (stress corrosion). The material model implements continuum damage mechanics theory through the introduction of a scalar damage parameter d, representing the extent of damage.

Corrosion of magnesium and its alloys is assumed to be a superposition of two types of non-uniform corrosion processes: stochastic pitting corrosion (d_p) and stress-driven corrosion (d_{sc}).

$$\frac{\partial d_p}{\partial t} = \frac{\delta_u}{L_e}\ K_u\ \lambda_p \tag{4.1}$$

$$\frac{\partial d_{sc}}{\partial t} = \frac{L_e}{\delta_{sc}}\ \left(\frac{S\ \sigma_{eq}}{1 - d_{sc}}\right)^R \tag{4.2}$$

if $\sigma_{eq} \geq\ \sigma_{th} > 0$

$$\frac{\partial d_{sc}}{\partial t} = 0 \tag{4.3}$$

if $\sigma_{eq} < \sigma_{th}$

The damage evolution laws Eq. 4.1, Eq. 4.2 and Eq. 4.3 describe the assumed evolution of the corrosion damage parameters in surface elements. λ_p is an element-specific dimensionless pitting parameter for which random values are assigned initially. K_u (h^{-1}) is a kinetic parameter for the corrosion process representing the uniform degradation rate, δ_u, δ_{sc} (mm) and L_e (mm) are material and FE model characteristic lengths respectively and σ_{eq} (MPa) represents a measure for the internal stress driving the stress corrosion process, e.g. the maximum principal stress. S ($mm^2h^{-0.5}N^{-1}$) and R (-) are constants related to the kinetics of the stress corrosion process depending on the corrosive environment. It is clear from equations 4.2 and 4.3 that stress corrosion only occurs when the equivalent stress σ_{eq} exceeds the value σ_{th} (MPa) and becomes more important as the internal stresses rise due to deformation.

Intrinsic to a continuum damage mechanics approach for modeling corrosion is the dependence of the results on the mesh element size. The inverse dependency on the characteristic length L_e in the damage evolution law Eq. 4.1 guarantees consistent degradation for different element sizes. The larger the volume of a finite element, the more time is required to evolve towards complete erosion of its mass. Grogan et al. [49] assign a value to δ_u consistent with grain sizes observed experimentally for the AZ31 alloy. Wu et al. [167, 179] on the other hand, adopt scaling of the numerical grid characteristic length with a relevant dimension of the corrosion process, namely the critical thickness of the corrosion film. Here, δ_u and δ_{sc} are tuned to achieve similar time scales for the pitting and stress corrosion processes.

Eventually, the contributions due to both pitting and stress corrosion are superposed linearly in order to evaluate the overall damage parameter d:

$$d = (1 - f)\ d_p + f\ d_{sc} \tag{4.4}$$

where $f = 0.5$ for convenience.

A random number generator, based on the standard Weibull distribution with probability density function (PDF) f(x), is used to assign λ_p values to all elements on the initial exposed surface. The probability of the value of λ_p to be in the range [a, b] is given by:

$$P\,[a\ \leq\ \lambda_p\ \leq\ b] = \int_a^b f(x)dx \tag{4.5}$$

$$f(x) = \gamma\ x^{\gamma-1}\ e^{-x^\gamma} \qquad x\ \geq\ 0,\ \gamma\ >\ 0 \tag{4.6}$$

γ is a dimensionless distribution shape factor characterizing the probability density function. Increasing values of γ result in a more symmetric and narrow range of λ_p values being assigned to surface elements, corresponding to a more homogeneous corrosion process (Fig. 4.1). For the modeling of non-uniform or localized corrosion, λ_p values are assigned according to a distribution with lower γ value.

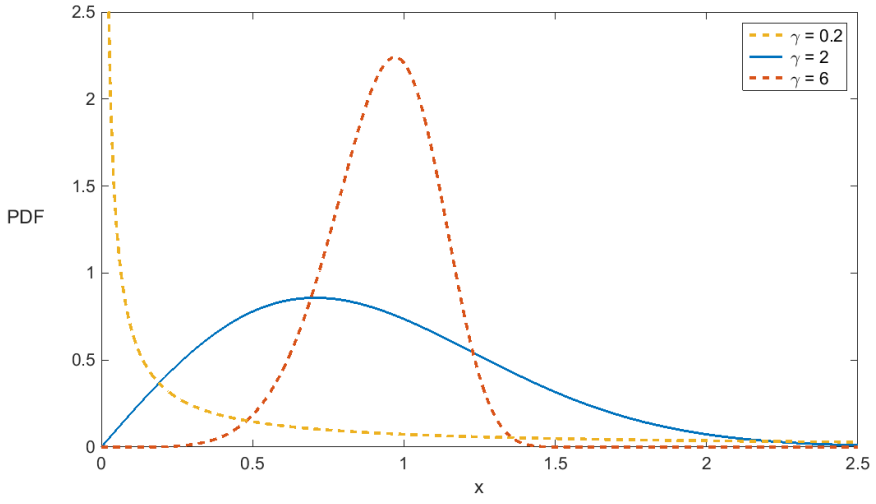

FIGURE 4.1: Probability density function (PDF) for a standard Weibull distribution. Increasing values of γ correspond to a more symmetric distribution of λ_p and more homogeneous corrosion.

A linear elastoplastic material behaviour with isotropic hardening is assumed for the magnesium stent alloy. An experimental stress-strain curve is used to describe the hardening behaviour of the undamaged material (Fig. 4.10). The influence of the damage parameter on the stress state σ is given by Eq. 4.7, where $\bar{\sigma}$ represents the stress tensor in the undamaged material. In damaged elements, the stress corresponding to a given strain value reduces as more damage is induced, governed by the evolution of the damage parameter d.

$$\sigma = (1 - d)\ \bar{\sigma} \tag{4.7}$$

In every iteration the strains and stresses are updated. By analogy with Grogan et al. [49] (implementation using Abaqus/Explicit) elements should be removed from the surface once the associated damage parameter effectively reaches its maximal value, modeling mass loss due to corrosive degradation. However, Abaqus/Standard does not allow for elements to be deleted. Instead, the mechanical properties of corroded elements are set to nearly zero, so that they do not longer contribute to the mechanics of the object. Subsequently, the underlying elements become subject to corrosion. When an element is effectively removed, the neighbouring elements (λ_p') inherit the value of the pitting parameter (Eq. 4.8). The dimensionless scaling parameter β controls pit growth acceleration. An element connectivity map is required to update the corrosion surface.

$$\lambda_p' = \beta\ \lambda_p \tag{4.8}$$

The implementation of this user-defined material model is given schematically in the following flowchart (Fig. 4.2). The damage subroutine is highlighted and the composing steps are shown in detail in Fig. 4.3. For implementation in FE code, both the constitutive equations and the damage evolution laws need to be converted to discrete approximations.

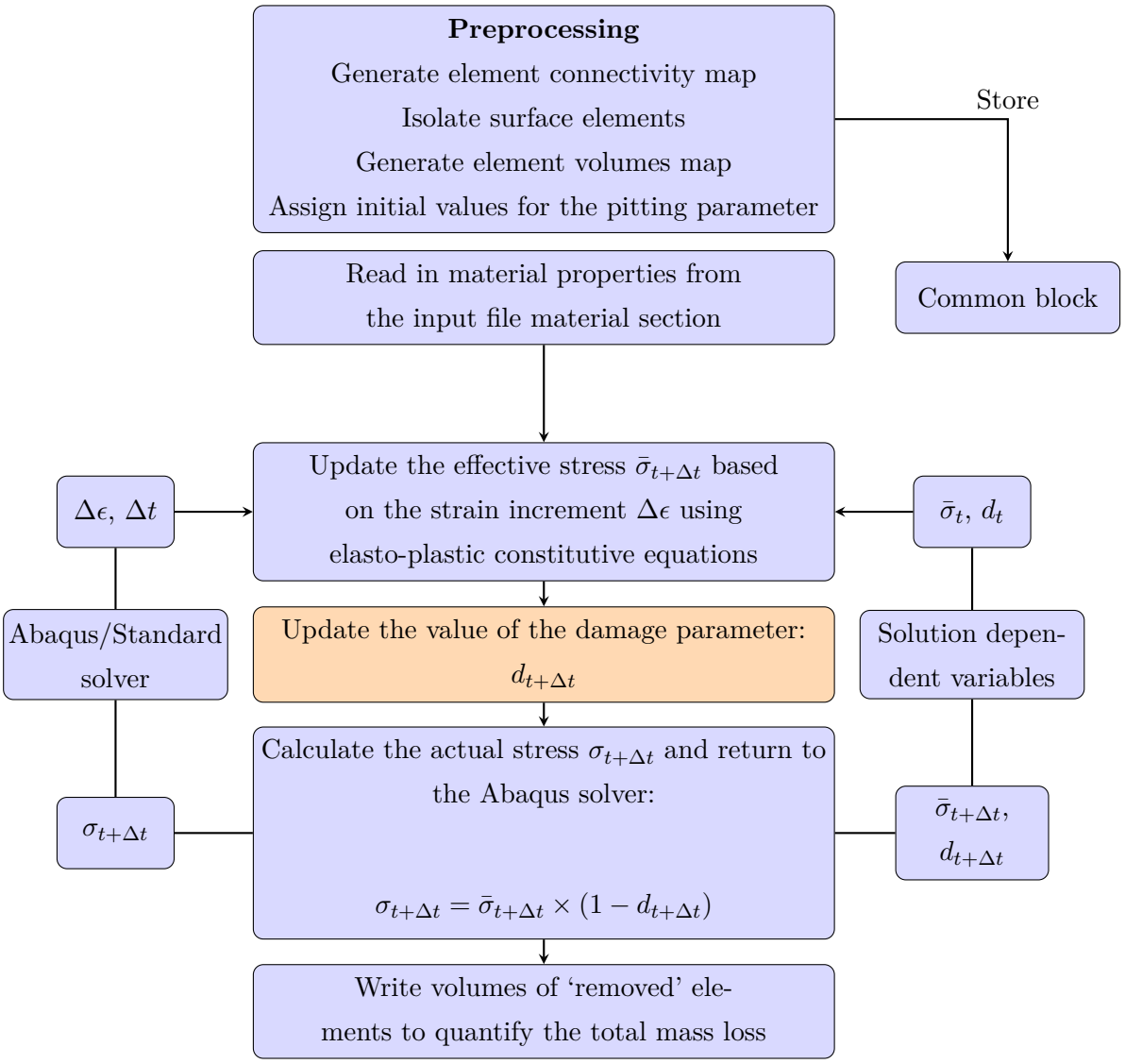

FIGURE 4.2: Schematic overview of the preprocessing steps and the corrosion model UMAT

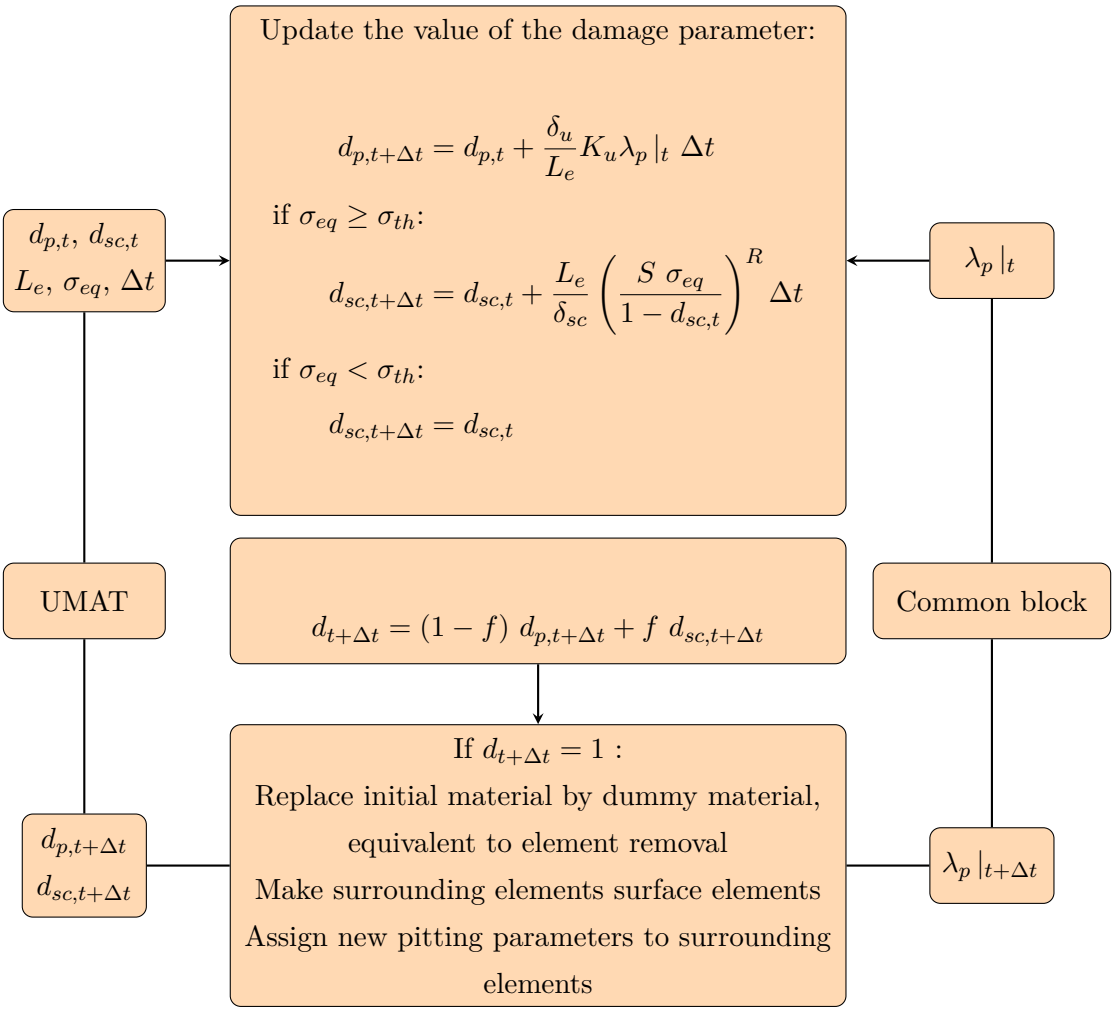

FIGURE 4.3: Schematic overview of the damage subroutine

4.3 Model calibration and validation

4.3.1 Simulation of experiments

Figures 4.4 through 4.6 illustrate virtual representations of the three types of experimental specimens used in experiments A, B and C (Section 3.1.2). The finite element mesh is shown in the outset.

The generated computational meshes are optimized for element uniformity. Finite elements with an aspect ratio close to 1 are most suited to model degradation-induced mass loss. Mesh convergence studies are conducted to guarantee minimal influence of the mesh on simulation results. The finite elements discretizing the volume of the geometries are progressively refined until the differences between consecutive results for the predicted corrosion rate and induced stresses become smaller than a tolerance of

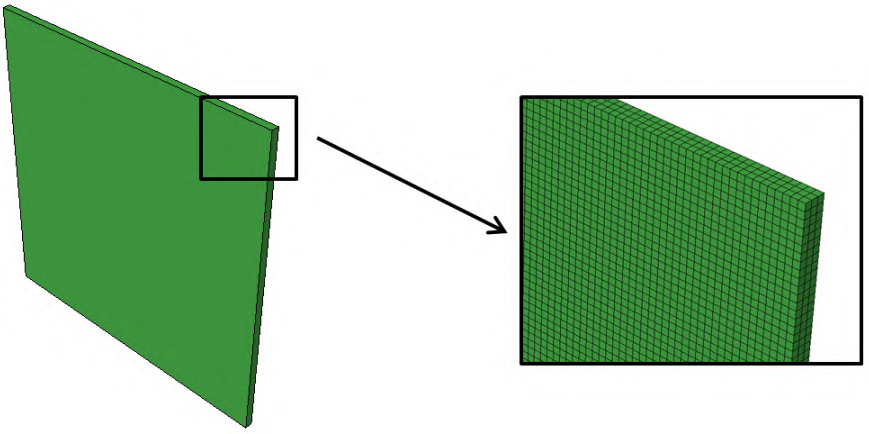

FIGURE 4.4: FE representation of the corroding foil specimen used in experiment A

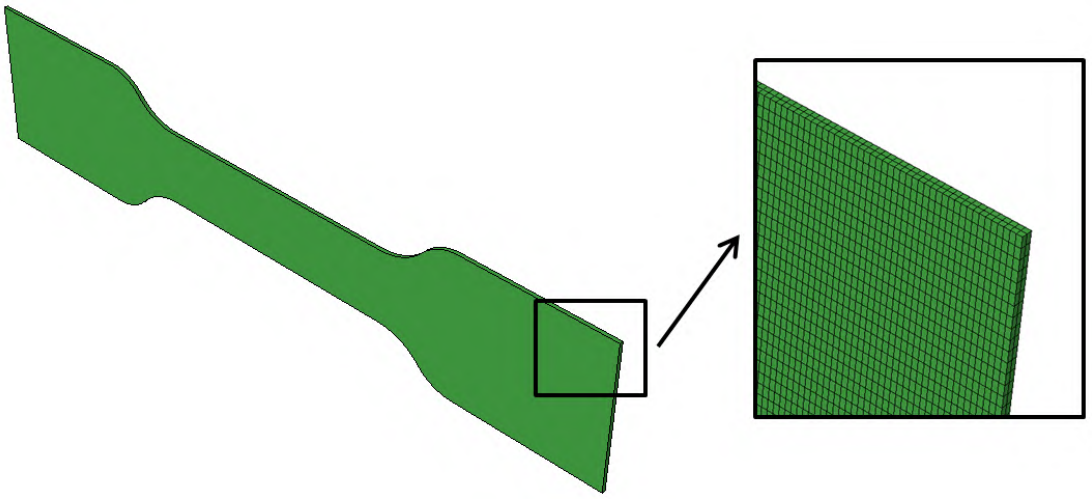

FIGURE 4.5: FE representation of the dog bone specimen used in experiment B

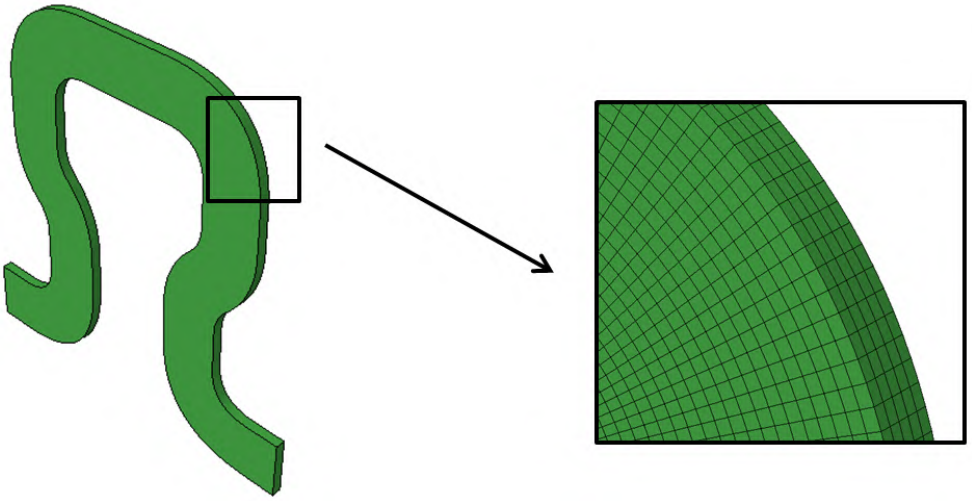

FIGURE 4.6: FE representation of the stent cell specimen used in experiment C

10%. The results of these analyses are summarized in Table 4.1. The element type used in simulations implementing corrosion modeling is an 8-node linear brick (C3D8)

without application of reduced integration (cf. C3D8R), as this method would require user-definition of the hourglass stiffness.

Experiment	Geometry	Simulation conditions	Number of elements (-)	Element characteristic length (mm)	Element type
A	Cuboid	Corr	43 200	0.144	C3D8
B	Dog bone	Mech	3920	0.433	C3D8R
		Corr	31 360	0.217	C3D8
C	Stent cell	Mech	2272	0.217	C3D8R
		Corr	38 000	0.087	C3D8

TABLE 4.1: FE meshes generated to discretize the specimen geometries used in experiment A, B and C (Mech: Purely mechanical modeling, Corr: Corrosion modeling)

In order to reproduce the results obtained in experiments A and B, corrosive degradation is simulated for different periods of time: 1h, 3h, 6h, 24h, 48h, 72h and 96h (Fig. 4.7). In a second step, tensile loading of the dog bone is achieved by imposing a displacement boundary condition on one end, while fixing the other (Fig. 4.9). To ensure an unambiguous problem definition, nodes in these plane sections are restrained in two directions orthogonal (y,z) to the loading direction (x). Tensile loading of the stent strut is simulated in the same way (Fig. 4.12). Afterwards, corrosion is allowed to occur (Fig. 4.13). Maximally 1000 time increments are used in the analysis. Additional refinement of the time step size is verified to have only a marginal effect on the simulation results.

4.3.2 Calibration strategy

In order to properly calibrate the corrosion model, material model parameters and degradation constants are tuned by fitting the FE simulation results to the collected experimental data. The first requirement is that the mass loss versus time curve predicted by the model corresponds qualitatively to the trend observed in experiment A. The condition of the evolution of mass loss in time having to match the course observed experimentally, allows to determine γ and β. Second, the simulated average corrosion rate should quantitatively match the experimental value, which enables to set a value on the uniform degradation rate parameter K_u for given values of γ and β. Third, the model should properly capture the corrosion-induced decrease in specimen mechanical integrity measured in experiment B.

4.4 Results and discussion

4.4.1 Determination of corrosion rate (A)

Fig. 4.7 demonstrates the evolution of the damage parameter throughout the specimen volume as a function of corrosion time. The numerical framework successfully simulates pitting-like material loss.

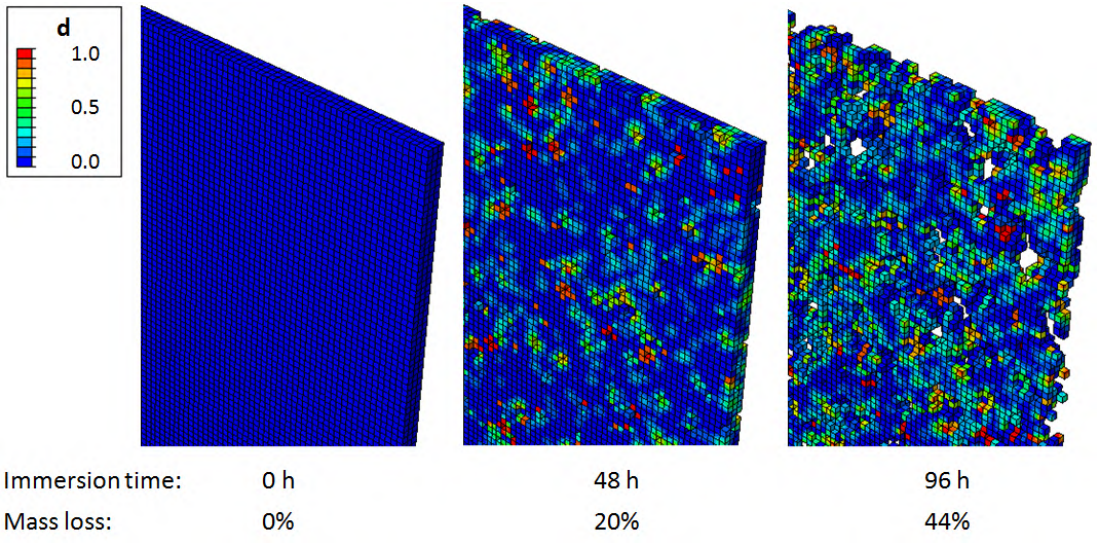

FIGURE 4.7: FE simulation predictions for experiment A. The color code represents the value of the damage parameter d or the degree of corrosion-induced damage.

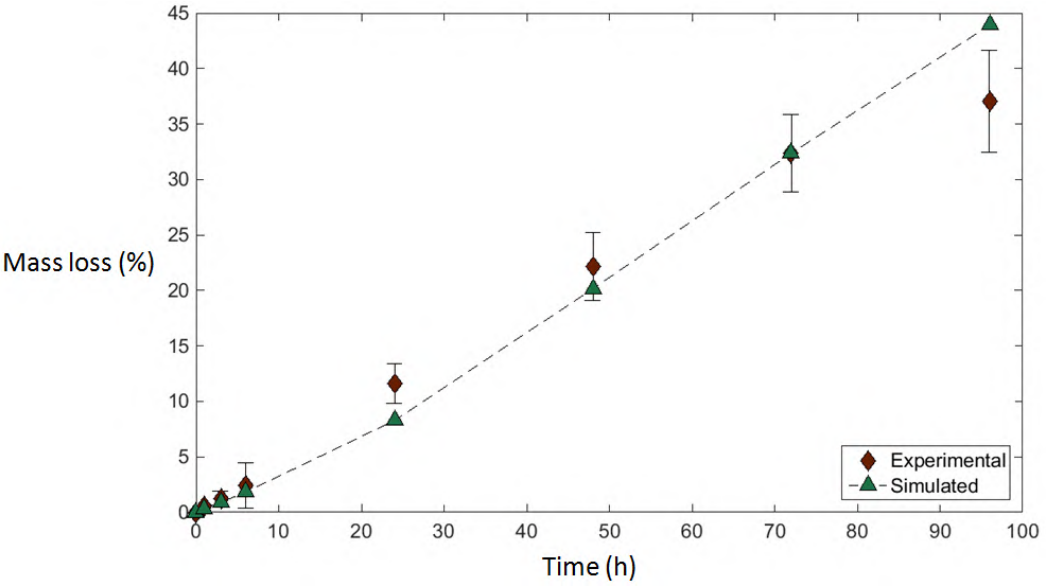

FIGURE 4.8: Percentage of mass lost over time as measured in experiment A and corresponding FE simulation predictions.
Error bars represent a single standard deviation from the mean (n=4).

In order to reproduce the experimentally observed corrosion rate, the FE model predictions are fitted to the mass loss measurements performed in experiment A (Section 3.3.1). The corrosion model is able to reproduce the two phase linear mass loss trend as a function of time (Fig. 4.8).

4.4.2 Effect of corrosion on mechanical properties (B)

The simulation results corresponding to experiment B are shown in Fig. 4.9. First, the gauge region is subject to corrosion. Next, the tensile stress-strain behaviour is evaluated.

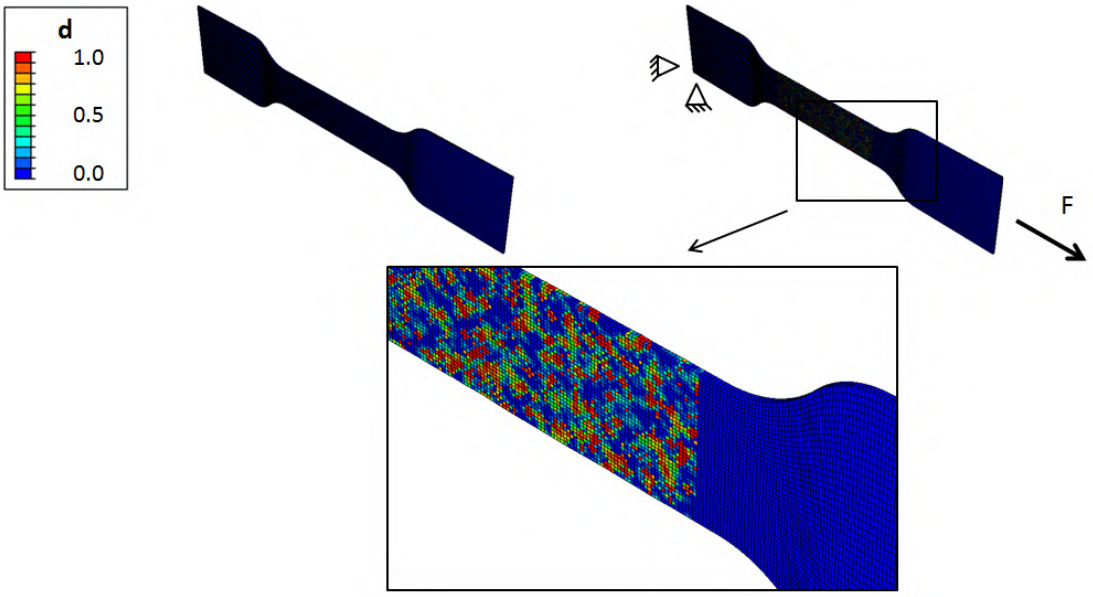

FIGURE 4.9: FE simulation prediction for experiment B, with indication of loading direction and boundary conditions. The color code represents the value of the damage parameter d or the degree of corrosion-induced damage.

Given the good fit between the FE predictions and experimental data (Fig. 4.10), the numerical framework captures the effect of a specific degree of corrosion-induced damage on the mechanical properties of the material relatively well. The reduction in ultimate tensile strength (UTS) with mass loss, both measured and simulated, is apparent from Fig. 4.11.

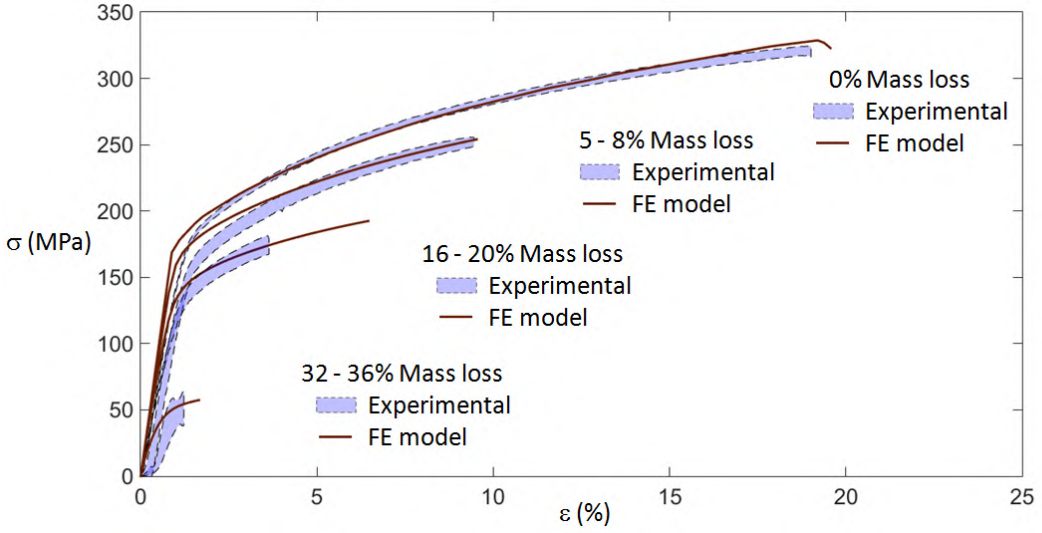

FIGURE 4.10: True stress-strain curves for different degrees of corrosion-induced mass loss as measured in experiment B and corresponding FE simulation predictions

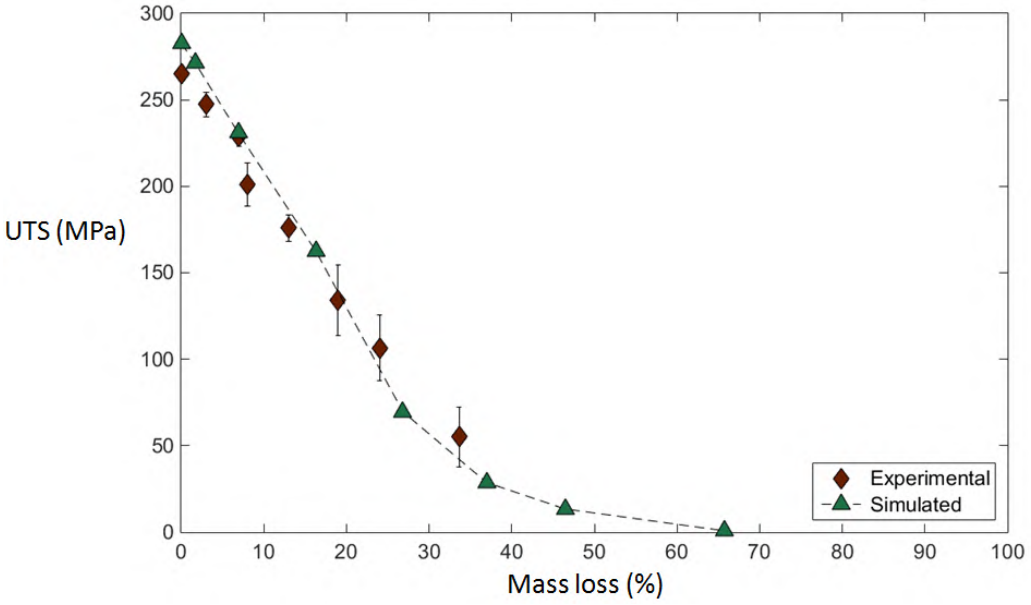

FIGURE 4.11: Ultimate tensile strength (UTS) as a function of corrosion-induced mass loss as measured in experiment B and corresponding FE simulation predictions. Error bars represent a single standard deviation from the mean (n=6).

4.4.3 Influence of a tensile load on corrosion (C)

The FE prediction of the stresses (maximal principal stress) induced in the material due to tensile loading is shown in Fig. 4.12. Slight differences in the corrosion process due to induced stresses are predicted by the corrosion model implementing both pitting and stress corrosion concepts (Fig. 4.13).

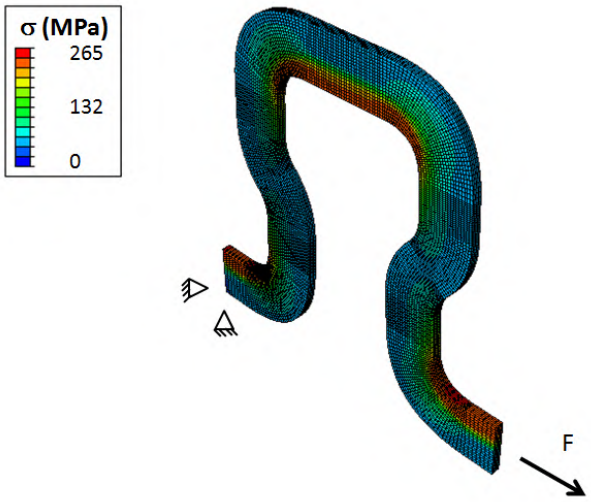

FIGURE 4.12: FE simulation prediction for the stresses induced in experiment C, with indication of loading direction and boundary conditions

No evidence of stress-induced changes in the rate of corrosion was observed experimentally (Section 3.3.3). Because of the convex combination, coefficients $f \geq 0$, $1 - f \geq 0$ and $\sum = 1$, of both damage parameters d_p and d_{sc} in Eq. 4.4, such effects are not incorporated in the modeling framework either. In the current formulation, with $f = 0.5$, the pitting and stress corrosion evolution laws contribute equally to the scalar damage field.

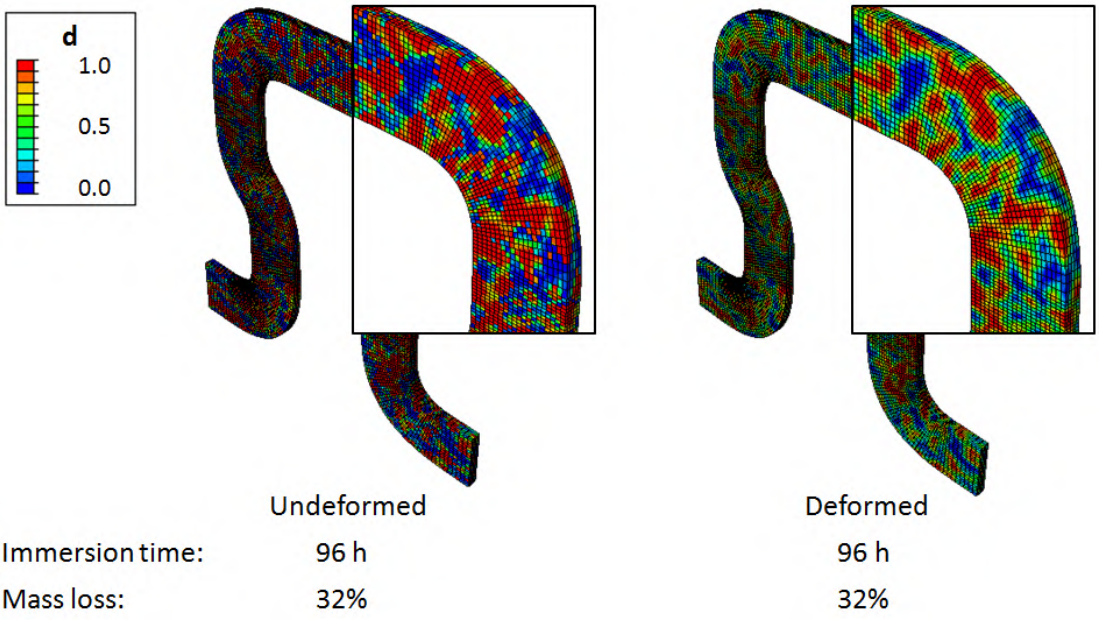

FIGURE 4.13: FE simulation predictions for experiment C. The color code represents the value of the damage parameter d or the degree of corrosion-induced damage.

4.4.4 Calibrated model parameters

A set of values for the corrosion model parameters allowing for a good fit of the experimental data collected in this study is shown in Table 4.2. Values reported by other authors are included for comparison.

Parameter	Calibrated value	Grogan et al.	Wu et al.
L_e (mm)	FE characteristic length	0.07	-
δ_u (mm)	0.100	0.017	0.100
δ_{sc} (mm)	0.067	n/a	0.070
K_u (h^{-1})	0.00650	0.00042	0.00500
γ (-)	0.2	0.2	n/a
β (-)	0.5	0.8	n/a
σ_{th} (MPa)	80	n/a	80
S ($mm^2\, h^{-0.5}\, N^{-1}$)	0.003	n/a	0.007
R (-)	2	n/a	2
Source		[49]	[167]

TABLE 4.2: Calibrated parameter values for the damage model description of Mg AZ31 pitting and stress corrosion

4.5 Model limitations

The purely phenomenological foundation of the model for pitting and stress corrosion implies a number of limitations. First, the continuum damage mechanics framework does not capture physical processes related to the electrochemical surface reactions or species evolution and diffusion. Therefore, the model is specific to a given metal alloy and solution composition. Recalibration is required as soon as another material or corrosion medium is considered.

Second, the effect of precipitates or grain size on the corrosion process is not taken into account, making the model predictions specific to one particular microstructure.

Another important limitation is the fact that tissue coverage of the material is not modeled. In reality, layers of cells and proteins are expected to affect mass transport as well as exposure to flow.

Finally, since the effect of dynamic loading conditions on corrosion is neglected, the possible reduction in mechanical integrity due to corrosion fatigue is not captured by the model.

Chapter 5

Modeling biodegradable magnesium stent mechanics

5.1 Methods

By analogy with Section 4.1 the damage model is implemented through a Fortran user subroutine or UMAT compatible with the finite element solver Abaqus/Standard (Dassault Systèmes, USA). Meshed generic stent geometries are readily created by means of the Python based open-source software pyFormex (bioMMeda, Ghent University). Finite element simulations are run on a high performance Linux computing cluster (184 CPU's) dedicated to computational mechanics.

5.2 Model development

The continuum damage mechanics corrosion modeling framework described in Chapter 4 is calibrated using experimental data for the AZ31 magnesium alloy (Chapter 3). Here, the developed corrosion model is applied to the FE modeling of realistic stent mechanics.

5.2.1 Stent geometry

The free expansion and subsequent degradation of a degradable metal stent is modeled. The reference stent geometry is the DREAMS (Drug-Eluting Absorbable Metal Stent) design by Biotronik (Fig. 3.3). Only the stent substrate material is modeled, so no coating is included in the analysis. Fig. 5.1 shows the FE geometry. The stent has an

initial diameter of 1.8 mm and a length of 10 mm. Both the strut width and strut height are 100 μm.

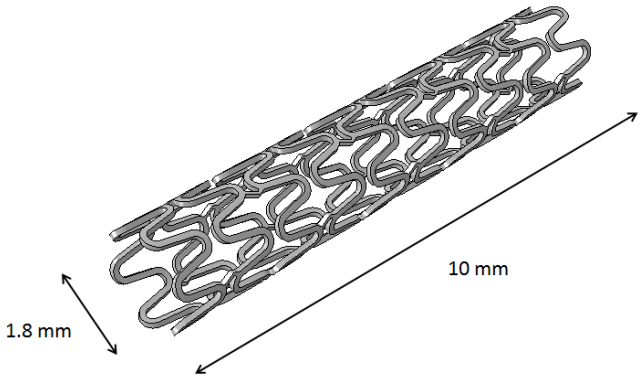

FIGURE 5.1: Stent geometry generated with the pyFormex software

5.2.2 Stent deployment and degradation

In this analysis, abstraction is made of the expansion balloon and the delivery system. Instead, radial displacements are imposed on rigid cylindrical surfaces. De Beule et al. [180] have shown that modeling stent deployment by means of rigid surfaces under displacement control significantly reduces computational cost, without inducing a substantial error with respect to the stent strut configuration at the end of the procedure. Since the main interest is in the buildup of stresses in the stent material and their effect on the corrosion attack, these simplifications are considered acceptable.

The simplified stent deployment simulation comprises the following steps:

1. Crimping
2. Elastic recoil
3. Expansion
4. Elastic recoil
5. Corrosion ($\Delta t = 0h - 96h$)
6. Radial strength evaluation

First, the stent with an initial diameter of 1.8 mm, is crimped to a minimal diameter equal to 1.0 mm. Next, the device is allowed to recoil (outward), expanded to a nominal diameter equal to 2.7 mm, followed by a second recoil phase (inward) (Fig. 5.2). The

following step comprises degradation of the deployed stent. Different corrosion time periods are simulated. After the free expansion and degradation phases, another step is implemented in order to quantify the radial strength of the device (Section 5.2.3).

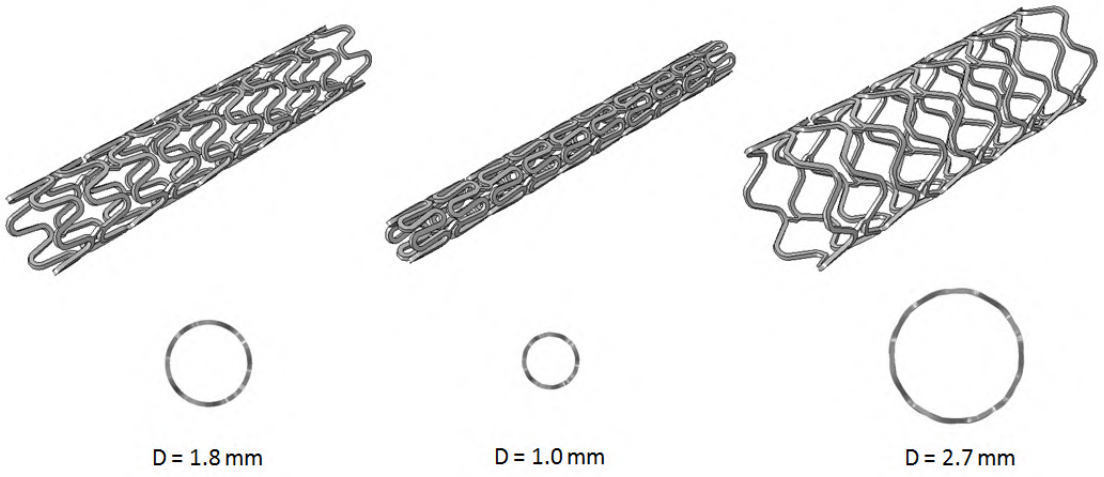

FIGURE 5.2: The initial stent configuration (left) and FE predictions for the configuration after crimping (middle) and after expansion (right)

The FE stent model is meshed with 200 448 C3D8 elements. In order to limit the computational expense, two interconnected rings are taken to represent the entire geometry. As a consequence, the mesh size is reduced to 39 636 elements. The number of SFM3D8 surface elements required to discretize the crimping and expansion surfaces is low. Here, only six elements are generated along the circumference of the cylindrical surfaces.

Surface-to-surface contact between the surfaces and the inner and outer stent surfaces is modeled. Elastic recoil is accounted for by removing the contact at the end of the crimping and expansion phases.

For the definition of boundary and loading conditions, a cylindrical coordinate system (R,T,Z) is introduced. R is the radial, T the circumferential and Z the longitudinal or axial direction. A couple of boundary conditions are imposed on three outer nodes on one end of the stent, positioned symmetrically along the circumference of the stent. Displacement of these nodes in both the axial and circumferential direction is precluded. Alternatively, the nodes could be fixed axially while defining a tangential friction factor μ (-). The friction factor is defined as the ratio of the frictional force F_{fr} to the normal force F_n (Eq. 5.1).

$$F_{fr} = \mu \, F_n \tag{5.1}$$

with $0 < \mu < 2$

The nodes on the rigid surfaces are restrained both axially and circumferentially. Displacements are imposed in order to radially contract and expand these surfaces, representative for the crimping of the stent and the controlled inflation of the balloon.

5.2.3 Evaluation of the radial strength

The radial strength (RS) of the investigated stent is evaluated for different degrees of corrosion-induced damage. Radial compression of the stent is again imposed through the introduction of a cylindrical shell under displacement control (Fig. 5.3). The collapse behaviour of the stent is characterized by virtue of the reaction force-displacement curve. The radial strength is derived from the reaction force value for which there is a sudden reduction in the stent diameter or, if no clear point of collapse exists, for which the diameter loss equals 10%. The radial stiffness constitutes an alternative measure that provides useful information about the condition and performance of both permanent and degradable stent devices. The stiffness can be derived from the initial compression behaviour (force-displacement curve).

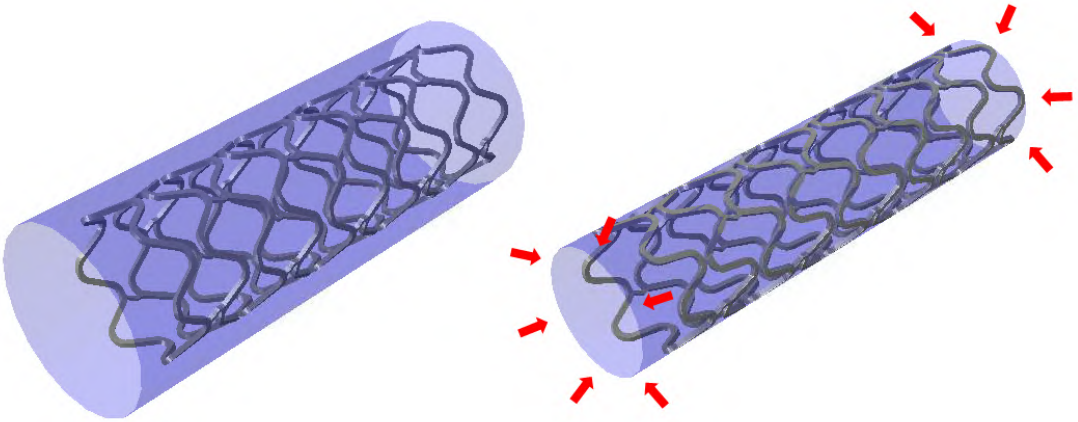

FIGURE 5.3: Representation of the approach to evaluate the radial strength of the stent. The arrows indicate the radial contraction of the cylindrical shell.

5.3 Results and discussion

The simulation results for the stresses induced in the stent material upon deployment and the pitting-like mass loss due to corrosion are shown in Fig. 5.4.

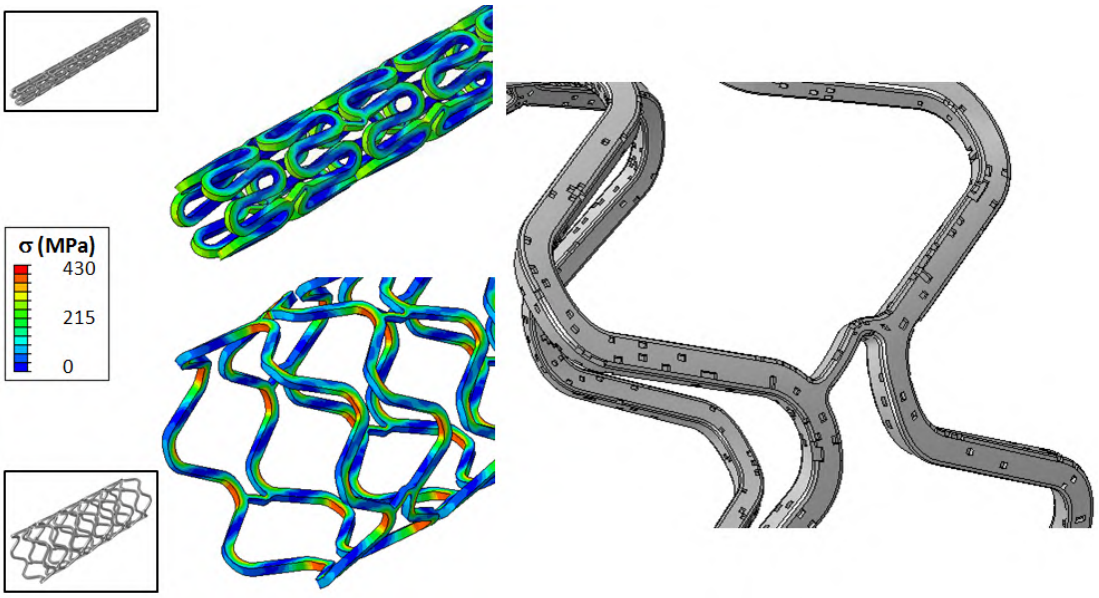

FIGURE 5.4: FE simulation predictions for the stresses induced in the stent material upon deployment (left) and the pitting corrosion process for 8.5 % mass loss (right)

Fig. 5.5 illustrates the predicted loss in stent radial strength for low percentages of mass loss. The intact device withstands a maximal load of 0.08 MPa. This collapse pressure corresponds very well to the value for the Magic stent (Biotronik) reported by Erbel et al. [27]. The collapse pressure predicted for the investigated magnesium stent is significantly lower than values for SS 316L and CoCr L605 stent devices measured experimentally (0.13 - 0.25 MPa) [181].

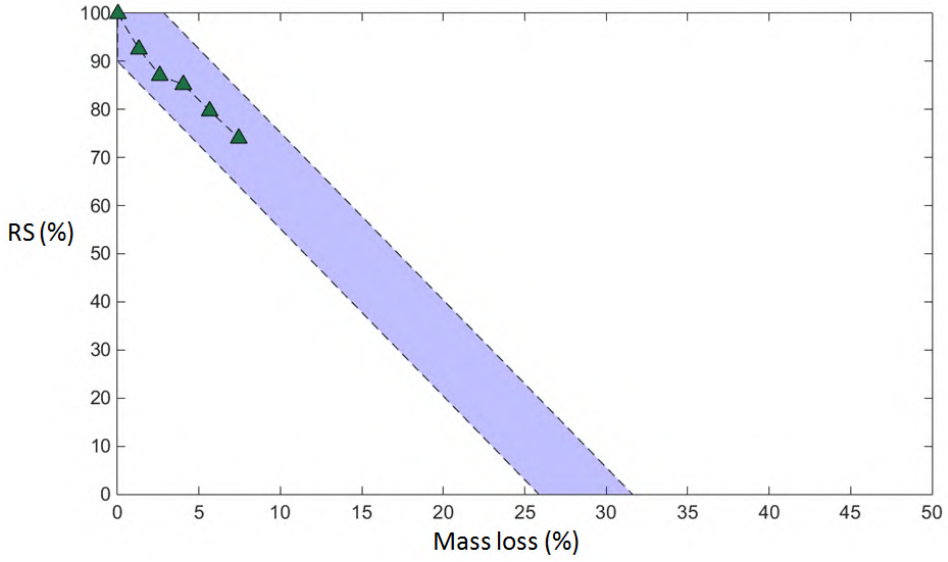

FIGURE 5.5: FE simulation predictions for the radial strength (RS) of the stent as a function of corrosion-induced mass loss. The blue shaded area indicates a linear extrapolation of the trend resolved for low percentages of mass loss.

The proposed approach has only proven suitable to evaluate the stent radial strength for low percentages of mass loss. The initial reduction is shown to be linear. 7.5% mass loss evokes a 25% decrease in the radial strength. For higher degrees of material loss, the simulations are terminated due to convergence issues, so no quantification is possible. To resolve these issues, further revision of the UMAT code and tweaking of the simulation conditions are required.

5.4 Validation

No validation study is conducted to assess the accuracy of the finite element computational model. The relevance of the FE results obtained for the stent radial strength as a function of corrosion mass loss could be validated by performing the crimping and free expansion of magnesium stents, immersing them in a corrosive environment, quantifying the mass loss and eventually determining the radial strength. Compression, expansion and measurement of reaction forces can be carried out by means of test systems such as the one illustrated in Fig. 5.6.

FIGURE 5.6: The RX550/650 (Machine Solutions) designed to measure and record radial reactive force during expansion and compression of interventional devices [182]

5.5 Limitations

In vivo, the deployed stent is subject to cyclic loading due to pulsatile blood flow. Given the static simulation conditions, failure due to fatigue is not accounted for in this work.

Stent strut dimensions typically lie within the range 50-150 μm. For some materials, this implies that there are only a few metallic grains throughout the cross-section of the struts. As such, microscale phenomena or size effects may become important and continuum plasticity theory may not fully capture the mechanical behaviour of the material [45]. Mostly, experimental stress-strain data are collected from tensile testing of large-size specimens. However, for structures with dimensions in the μm range failure stresses and strains are size dependent. Microscale modeling based on crystal plasticity theory has been implemented by Harewood and McHugh [183] to investigate size effects for realistic stent strut geometries and representative loading modes.

Since the primary focus is on the application of corrosion modeling in combination with realistic stent mechanics, no blood vessel model is included in this analysis, reducing the computational expense. Also, abstraction is made of the inflatable expansion balloon and associated delivery system (catheter). Deployment by means of rigid cylindrical surfaces has been shown to produce a good approximation of the stent configuration achieved in more computationally expensive wrapped balloon simulations [180].

Chapter 6

Conclusion and future work

6.1 Conclusion

Current in vitro test systems applying simplifying conditions allow to screen qualitatively for new stent alloys. However, it is not possible to predict the in vivo corrosion behaviour accurately. Simulation of in vivo conditions regarding exact body fluid composition, transport processes and mechanical stresses is troublesome. The higher dissolution rates of magnesium alloys often observed in vitro are probably due to higher concentrations of chloride and the absence of proteins and cells in the electrolyte solution applied. Selection of an appropriate medium as well as physiological flow conditions is key to transfering conclusions drawn from in vitro corrosion tests to in vivo application.

Considering the limited complexity of the in vitro test environment used, it cannot be expected to reproduce with great accuracy in vivo degradation processes. However, the efforts in this work clearly demonstrate the feasibility of using in vitro experimental data, collected during relatively simple tests, to calibrate a theoretical corrosion model dedicated to FE modeling of stent mechanics.

In general there are four different methods to evaluate the corrosion rate of metallic materials: mass loss, hydrogen evolution, ion release concentration and electrochemical corrosion current measurement. In this work, the hydrogen evolution method is selected to quantify the rate of corrosion, because of its robustness for dynamic measurements. The pitting and stress corrosion model is able to predict the mass loss time course.

The experimental results indicate a significant reduction in mechanical integrity, even for modest corrosion-induced mass losses. The modeling framework captures the effect of corrosion on the mechanical properties of the material very well. A good fit is found

between experimental stress-strain curves and the stress-strain behaviour predicted by the FE model.

The continuum damage mechanics framework combining pitting and stress corrosion modeling for the AZ31 alloy is successfully applied to a realistic stent geometry. Both deployment and degradation of the stent are simulated. Eventually, the loss in stent radial strength for low percentages of mass loss is predicted.

6.2 Future trends in experimental characterisation

Since much of the inconsistency regarding the degradation characteristics of Mg alloys stems from the choice of the test medium, adoption of new standards for in vitro studies is desirable, applying experimental test conditions even more representative of the in vivo environment of endovascular devices: a pseudo-physiological solution with composition similar to human blood and a circulation system to mimic the in vivo flow conditions. The effects of protein adsorption and cell attachment on the corrosion process are largely unknown and should be studied in more detail. Finally, systematic evaluation of the cytotoxicity of novel alloys for biomedical implants is required in order to select the best performing materials.

6.3 Future trends in computational modeling

In the future, the current corrosion modeling framework has to be made more robust, so that it becomes generally applicable. In particular, the time scaling in the evolution laws for different types of corrosion should be studied in more detail.

A phenomenological model like the one applied in this work, requires recalibration for different stent materials and/or microstructures. Some authors have reported about physical modeling of the electrochemical and transport processes associated to the corrosion surface reaction. ALE adaptive meshing can be used to track moving corrosion interfaces. A comprehensive physical modeling framework would be applicable to any material, requiring only physical characteristics (e.g. rate constants, diffusion coefficients).

To prolonge the life time of the device, magnesium alloy stents are currently covered with a polymeric coating. New FE frameworks adopted to model the mechanics and degradation of these devices should implement realistic interaction between the substrate and coating.

Bibliography

[1] V. L. Roger. Epidemiology of myocardial infarction. *The Medical clinics of North America*, 91(4):537–52, July 2007.

[2] A. S. Go, D. Mozaffarian, V. L. Roger, E. J. Benjamin, et al. Heart disease and stroke statistics–2014 update: a report from the American Heart Association. *Circulation*, 129(3):28–292, January 2014.

[3] I. Sipahi, M. H. Akay, S. Dagdelen, A. Blitz, et al. Coronary artery bypass grafting vs percutaneous coronary intervention and long-term mortality and morbidity in multivessel disease: Meta-analysis of randomized clinical trials of the arterial grafting and stenting era. *JAMA Internal Medicine*, 174(2):223–30, February 2014.

[4] T. Wu and S. McCarthy. Coronary Arterial Drug-Eluting Stent: From Structure to Clinical. Technical report, Intech, 2012.

[5] P. Van De Bruaene. Personal communication (AZ Oudenaarde), 2014.

[6] Angioplasty and Stenting - NYC Surgical Associates, www.nycsurgical.net/womens-health/angioplasty-stenting, 2014.

[7] P. Serruys and P. de Jaegere. A comparison of balloon-expandable-stent implantation with balloon angioplasty in patients with coronary artery disease. *The New England Journal of Medicine*, 331(8):489–95, 1994.

[8] D. Fischman and M. Leon. A randomized comparison of coronary-stent placement and balloon angioplasty in the treatment of coronary artery disease. *The New England Journal of Medicine*, 331(8):496–501, 1994.

[9] M. Moravej and D. Mantovani. Biodegradable metals for cardiovascular stent application: interests and new opportunities. *International journal of molecular sciences*, 12(7):4250–70, January 2011.

[10] P. Erne, M. Schier, and T. J. Resink. The road to bioabsorbable stents: Reaching clinical reality? *Cardiovascular and interventional radiology*, 29(1):11–16, 2006.

[11] D. Holmes and D. Kereiakes. Stent thrombosis. *Journal of the American College of Cardiology*, 56(17):1357–65, 2010.

[12] P. K. Shah. Inflammation, neointimal hyperplasia, and restenosis: As the leukocytes roll, the arteries thicken. *Circulation*, 107(17):2175–7, May 2003.

[13] C. Stettler, S. Wandel, S. Allemann, A. Kastrati, et al. Outcomes associated with drug-eluting and bare-metal stents: A collaborative network meta-analysis. *Lancet*, 370(9591):937–48, September 2007.

[14] A. Abizaid and J. R. Costa. New drug-eluting stents: An overview on biodegradable and polymer-free next-generation stent systems. *Circulation. Cardiovascular interventions*, 3(4):384–93, August 2010.

[15] M. Vorpahl, R. Virmani, E. Ladich, and A. V. Finn. Vascular remodeling after coronary stent implantation. *Minerva cardioangiologica*, 57(5):621–8, October 2009.

[16] D. Moliterno. Healing Achilles-sirolimus versus paclitaxel. *The New England Journal of Medicine*, 353(7):724–7, 2005.

[17] J. E. Sousa. Sirolimus-Eluting Stent for the Treatment of In-Stent Restenosis: A Quantitative Coronary Angiography and Three-Dimensional Intravascular Ultrasound Study. *Circulation*, 107(1):24–27, December 2002.

[18] J. A. Ormiston and P. W. S. Serruys. Bioabsorbable coronary stents. *Circulation. Cardiovascular interventions*, 2(3):255–60, June 2009.

[19] R. Waksman. Biodegradable stents: They do their job and disappear. *The Journal of Invasive Cardiology*, 18(2):70–74, 2006.

[20] R. Waksman. Promise and challenges of bioabsorbable stents. *Catheterization and Cardiovascular Interventions*, 70(3):407–14, September 2007.

[21] S. Venkatraman, F. Boey, and L. L. Lao. Implanted cardiovascular polymers: Natural, synthetic and bio-inspired. *Progress in Polymer Science*, 33(9):853–874, September 2008.

[22] R. Waksman and R. Pakala. Biodegradable and Bioabsorbable Stents. *Current Pharmaceutical Design*, 16(36):4041–4051, December 2010.

[23] R. Waksman. The disappearing stent: When plastic replaces metal. *Circulation*, 125(19):2291–4, May 2012.

[24] S. Ramcharitar and P. W. Serruys. Fully Biodegradable Coronary Stents. *American Journal of Cardiovascular Drugs*, 8(5):305–314, 2008.

[25] S. Nishio, K. Kosuga, K. Igaki, M. Okada, et al. Long-Term (>10 Years) clinical outcomes of first-in-human biodegradable poly-l-lactic acid coronary stents: Igaki-Tamai stents. *Circulation*, 125(19):2343–53, May 2012.

[26] A. Lupi, G. Gabrio Secco, A. Rognoni, M. Lazzero, et al. Meta-analysis of bioabsorbable versus durable polymer drug-eluting stents in 20,005 patients with coronary artery disease: An update. *Catheterization and Cardiovascular Interventions*, 83(6):193–206, May 2014.

[27] R. Erbel, C. Di Mario, J. Bartunek, J. Bonnier, et al. Temporary scaffolding of coronary arteries with bioabsorbable magnesium stents: A prospective, non-randomised multicentre trial. *Lancet*, 369(9576):1869–75, June 2007.

[28] R. Waksman, R. Erbel, C. Di Mario, J. Bartunek, et al. Early- and Long-Term Intravascular Ultrasound and Angiographic Findings After Bioabsorbable Magnesium Stent Implantation in Human Coronary Arteries. *JACC: Cardiovascular Interventions*, 2(4):312–320, April 2009.

[29] C. M. Campos, T. Muramatsu, J. Iqbal, Y.-J. Zhang, et al. Bioresorbable drug-eluting magnesium-alloy scaffold for treatment of coronary artery disease. *International journal of molecular sciences*, 14(12):24492–500, January 2013.

[30] M. Haude, R. Erbel, P. Erne, S. Verheye, et al. Safety and performance of the drug-eluting absorbable metal scaffold (DREAMS) in patients with de-novo coronary lesions: 12 month results of the prospective, multicentre, first-in-man BIOSOLVE-I trial. *Lancet*, 381(9869):836–44, March 2013.

[31] R. Waksman. Absorbable Metal Stent, Clinical Update and DREAMS: Concept and preclinical Data, 2007.

[32] P. Zartner, R. Cesnjevar, H. Singer, and M. Weyand. First successful implantation of a biodegradable metal stent into the left pulmonary artery of a preterm baby. *Catheterization and Cardiovascular Interventions*, 66(4):590–4, December 2005.

[33] D. Schranz, P. Zartner, I. Michel-Behnke, and H. Akintürk. Bioabsorbable metal stents for percutaneous treatment of critical recoarctation of the aorta in a newborn. *Catheterization and Cardiovascular Interventions*, 67(5):671–3, May 2006.

[34] P. Peeters, M. Bosiers, J. Verbist, K. Deloose, et al. Preliminary results after application of absorbable metal stents in patients with critical limb ischemia. *Journal of Endovascular Therapy*, 12(1):1–5, February 2005.

[35] M. Peuster, P. Beerbaum, F.-W. Bach, and H. Hauser. Are resorbable implants about to become a reality? *Cardiology in the young*, 16(2):107–16, April 2006.

[36] M. Bosiers, P. Peeters, O. D'Archambeau, J. Hendriks, et al. AMS INSIGHT - Absorbable metal stent implantation for treatment of below-the-knee critical limb ischemia: 6-month analysis. *Cardiovascular and interventional radiology*, 32(3):424–35, May 2009.

[37] M. Peuster. A novel approach to temporary stenting: Degradable cardiovascular stents produced from corrodible metal—results 6-18 months after implantation into New Zealand white rabbits. *Heart*, 86(5):563–569, November 2001.

[38] Y. Onuma, J. Ormiston, and P. W. Serruys. Bioresorbable Scaffold Technologies. *Circulation Journal*, 75(3):509–520, January 2011.

[39] S. Zhu, N. Huang, L. Xu, Y. Zhang, et al. Biocompatibility of pure iron: In vitro assessment of degradation kinetics and cytotoxicity on endothelial cells. *Materials Science and Engineering: C*, 29(5):1589–1592, June 2009.

[40] K. Sternberg, M. Gratz, K. Koeck, J. Mostertz, et al. Magnesium used in bioabsorbable stents controls smooth muscle cell proliferation and stimulates endothelial cells in vitro. *Journal of biomedical materials research. Part B, Applied biomaterials*, 100(1):41–50, January 2012.

[41] S. Zhang, J. Li, Y. Song, C. Zhao, et al. In vitro degradation, hemolysis and MC3T3-E1 cell adhesion of biodegradable Mg–Zn alloy. *Materials Science and Engineering: C*, 29(6):1907–1912, August 2009.

[42] J. A. Grogan, S. B. Leen, and P. E. McHugh. Comparing coronary stent material performance on a common geometric platform through simulated bench testing. *Journal of the mechanical behavior of biomedical materials*, 12:129–38, August 2012.

[43] G. Mani, M. D. Feldman, D. Patel, and C. M. Agrawal. Coronary stents: A materials perspective. *Biomaterials*, 28(9):1689–710, March 2007.

[44] X. B. Zhang, G. Y. Yuan, X. X. Fang, Z. Z. Wang, et al. Effects of solution treatment on yield ratio and biocorrosion behaviour of as-extruded Mg–2·7Nd–0·2Zn–0·4Zr alloy for cardiovascular stent application. *Materials Technology*, 28(3):155–158, May 2013.

[45] B. P. Murphy, P. Savage, P. E. McHugh, and D. F. Quinn. The Stress–Strain Behavior of Coronary Stent Struts is Size Dependent. *Annals of Biomedical Engineering*, 31(6):686–691, June 2003.

[46] P. Poncin, C. Millet, J. Chevy, and J. Proft. Comparing and optimizing Co-Cr tubing for stent applications. *Proceedings of the Materials and Processes for Medical Devices Conference*, 2004.

[47] B. J. O'Brien, J. S. Stinson, S. R. Larsen, M. J. Eppihimer, et al. A platinum-chromium steel for cardiovascular stents. *Biomaterials*, 31(14):3755–61, May 2010.

[48] X. N. Gu, W. R. Zhou, Y. F. Zheng, Y. Cheng, et al. Corrosion fatigue behaviors of two biomedical Mg alloys - AZ91D and WE43 - In simulated body fluid. *Acta biomaterialia*, 6(12):4605–13, December 2010.

[49] J. A. Grogan, B. J. O'Brien, S. B. Leen, and P. E. McHugh. A corrosion model for bioabsorbable metallic stents. *Acta biomaterialia*, 7(9):3523–33, September 2011.

[50] Y. Zong, G. Yuan, X. Zhang, L. Mao, et al. Comparison of biodegradable behaviors of AZ31 and Mg–Nd–Zn–Zr alloys in Hank's physiological solution. *Materials Science and Engineering: B*, 177(5):395–401, March 2012.

[51] X. Zhang, G. Yuan, L. Mao, J. Niu, et al. Biocorrosion properties of as-extruded Mg–Nd–Zn–Zr alloy compared with commercial AZ31 and WE43 alloys. *Materials Letters*, 66(1):209–211, January 2012.

[52] H. Hermawan, D. Dubé, and D. Mantovani. Developments in metallic biodegradable stents. *Acta biomaterialia*, 6(5):1693–7, May 2010.

[53] H. Hermawan, M. Moravej, D. Dubé, M. Fiset, et al. Degradation Behaviour of Metallic Biomaterials for Degradable Stents. *Advanced Materials Research*, 15-17:113–118, February 2007.

[54] M. Peuster, C. Hesse, T. Schloo, C. Fink, et al. Long-term biocompatibility of a corrodible peripheral iron stent in the porcine descending aorta. *Biomaterials*, 27(28):4955–62, October 2006.

[55] N. N. Aung and W. Zhou. Effect of grain size and twins on corrosion behaviour of AZ31B magnesium alloy. *Corrosion Science*, 52(2):589–594, February 2010.

[56] H. Wang, Y. Estrin, and Z. Zúberová. Bio-corrosion of a magnesium alloy with different processing histories. *Materials Letters*, 62(16):2476–2479, June 2008.

[57] M. Alvarez-Lopez, M. D. Pereda, J. A. del Valle, M. Fernandez-Lorenzo, et al. Corrosion behaviour of AZ31 magnesium alloy with different grain sizes in simulated biological fluids. *Acta biomaterialia*, 6(5):1763–71, May 2010.

[58] J. E. Gray-Munro, C. Seguin, and M. Strong. Influence of surface modification on the in vitro corrosion rate of magnesium alloy AZ31. *Journal of biomedical materials research. Part A*, 91(1):221–30, October 2009.

[59] C. Ye, Y. Zheng, S. Wang, T. Xi, et al. In vitro corrosion and biocompatibility study of phytic acid modified WE43 magnesium alloy. *Applied Surface Science*, 258(8):3420–3427, February 2012.

[60] G. Wu, J. M. Ibrahim, and P. K. Chu. Surface design of biodegradable magnesium alloys — A review. *Surface and Coatings Technology*, 233:2–12, October 2013.

[61] Z. Wen, C. Wu, C. Dai, and F. Yang. Corrosion behaviors of Mg and its alloys with different Al contents in a modified simulated body fluid. *Journal of Alloys and Compounds*, 488(1):392–399, November 2009.

[62] J. Wang, L. Wang, S. Guan, S. Zhu, et al. Microstructure and corrosion properties of as sub-rapid solidification Mg-Zn-Y-Nd alloy in dynamic simulated body fluid for vascular stent application. *Journal of materials science. Materials in medicine*, 21(7):2001–8, July 2010.

[63] G. Baril, C. Blanc, and N. Pebere. AC Impedance Spectroscopy in Characterizing Time-Dependent Corrosion of AZ91 and AM50 Magnesium Alloys Characterization with Respect to Their Microstructures. *Journal of the Electrochemical Society*, 148(12):489, December 2001.

[64] G. Song. Control of biodegradation of biocompatable magnesium alloys. *Corrosion Science*, 49(4):1696–1701, April 2007.

[65] A. Drynda, N. Deinet, N. Braun, and M. Peuster. Rare earth metals used in biodegradable magnesium-based stents do not interfere with proliferation of smooth muscle cells but do induce the upregulation of inflammatory genes. *Journal of biomedical materials research. Part A*, 91(2):360–9, November 2009.

[66] R. Köster, D. Vieluf, M. Kiehn, M. Sommerauer, et al. Nickel and molybdenum contact allergies in patients with coronary in-stent restenosis. *Lancet*, 356(9245):1895–7, December 2000.

[67] R. V. Marrey, R. Burgermeister, R. B. Grishaber, and R. O. Ritchie. Fatigue and life prediction for cobalt-chromium stents: A fracture mechanics analysis. *Biomaterials*, 27(9):1988–2000, March 2006.

[68] Y. Zhu, G. Wu, Y.-H. Zhang, and Q. Zhao. Growth and characterization of Mg(OH)2 film on magnesium alloy AZ31. *Applied Surface Science*, 257(14):6129–6137, May 2011.

[69] Rowan Technology Group: Galvanic Series, www.rowantechnology.com/technical-resources/galvanic-series, 2015.

[70] G. Song and A. Atrens. Understanding Magnesium Corrosion - A Framework for Improved Alloy Performance. *Advanced Engineering Materials*, 5(12):837–858, December 2003.

[71] F. Witte, N. Hort, C. Vogt, S. Cohen, et al. Degradable biomaterials based on magnesium corrosion. *Current Opinion in Solid State and Materials Science*, 12(5-6):63–72, October 2008.

[72] A. Atrens, M. Liu, and N. I. Zainal Abidin. Corrosion mechanism applicable to biodegradable magnesium implants. *Materials Science and Engineering: B*, 176(20):1609–1636, December 2011.

[73] Z. Zhen, T.-f. Xi, and Y.-f. Zheng. A review on in vitro corrosion performance test of biodegradable metallic materials. *Transactions of Nonferrous Metals Society of China*, 23(8):2283–2293, August 2013.

[74] C. Di Mario, H. Griffiths, O. Goktekin, N. Peeters, et al. Drug-eluting bioabsorbable magnesium stent. *Journal of interventional cardiology*, 17(6):391–5, December 2004.

[75] F. Witte, J. Fischer, J. Nellesen, H.-A. Crostack, et al. In vitro and in vivo corrosion measurements of magnesium alloys. *Biomaterials*, 27(7):1013–8, March 2006.

[76] Y. Ren, J. Huang, K. Yang, B. Zhang, et al. Study of bio-corrosion of pure magnesium. *Acta Metallurgica Sinica*, 41(11):1228–1232, 2005.

[77] C. Weber, G. Knörnschild, and L. Dick. The negative-difference effect during the localized corrosion of magnesium and of the AZ91HP alloy. *Journal of the Brazilian Chemical Society*, 14(4), 2003.

[78] J. Grogan. The Mechanical Performance of Permanent and Bioabsorbable Metal Stents, Phd. Thesis, September 2012.

[79] G. Song, A. Atrens, X. Wu, and B. Zhang. Corrosion behaviour of AZ21, AZ501 and AZ91 in sodium chloride. *Corrosion Science*, 40(10):1769–1791, October 1998.

[80] G. L. Song and A. Atrens. Corrosion Mechanisms of Magnesium Alloys. *Advanced Engineering Materials*, 1(1):11–33, September 1999.

[81] J. H. Nordlien. Morphology and Structure of Oxide Films Formed on MgAl Alloys by Exposure to Air and Water. *Journal of The Electrochemical Society*, 143(8):2564, August 1996.

[82] J. H. Nordlien. Morphology and Structure of Water-Formed Oxides on Ternary MgAl Alloys. *Journal of The Electrochemical Society*, 144(2):461, February 1997.

[83] W.-D. Mueller, M. F. L. de Mele, M. L. Nascimento, and M. Zeddies. Degradation of magnesium and its alloys: Dependence on the composition of the synthetic

biological media. *Journal of biomedical materials research. Part A*, 90(2):487–95, August 2009.

[84] M. Bobby Kannan, W. Dietzel, C. Blawert, A. Atrens, et al. Stress corrosion cracking of rare-earth containing magnesium alloys ZE41, QE22 and Elektron 21 (EV31A) compared with AZ80. *Materials Science and Engineering: A*, 480(1-2):529–539, May 2008.

[85] M. Bobby Kannan and R. Singh Raman. Evaluating the stress corrosion cracking susceptibility of Mg–Al–Zn alloy in modified-simulated body fluid for orthopaedic implant application. *Scripta Materialia*, 59(2):175–178, July 2008.

[86] X. Gu, Y. Zheng, Y. Cheng, S. Zhong, et al. In vitro corrosion and biocompatibility of binary magnesium alloys. *Biomaterials*, 30(4):484–98, February 2009.

[87] Y. Song, D. Shan, R. Chen, F. Zhang, et al. Biodegradable behaviors of AZ31 magnesium alloy in simulated body fluid. *Materials Science and Engineering: C*, 29(3):1039–1045, April 2009.

[88] Y. Xin, T. Hu, and P. K. Chu. In vitro studies of biomedical magnesium alloys in a simulated physiological environment: A review. *Acta biomaterialia*, 7(4):1452–9, April 2011.

[89] A. Yamamoto and S. Hiromoto. Effect of inorganic salts, amino acids and proteins on the degradation of pure magnesium in vitro. *Materials Science and Engineering: C*, 29(5):1559–1568, June 2009.

[90] R. Zeng, W. Dietzel, F. Witte, N. Hort, et al. Progress and Challenge for Magnesium Alloys as Biomaterials. *Advanced Engineering Materials*, 10(8):B3–B14, August 2008.

[91] P. S. Stewart. A review of experimental measurements of effective diffusive permeabilities and effective diffusion coefficients in biofilms. *Biotechnology and bioengineering*, 59(3):261–72, August 1998.

[92] W. D. Müller, M. L. Nascimento, M. Zeddies, M. Córsico, et al. Magnesium and its alloys as degradable biomaterials: corrosion studies using potentiodynamic and EIS electrochemical techniques. *Materials Research*, 10(1):5–10, March 2007.

[93] R. Rettig and S. Virtanen. Time-dependent electrochemical characterization of the corrosion of a magnesium rare-earth alloy in simulated body fluids. *Journal of biomedical materials research. Part A*, 85(1):167–75, April 2008.

[94] R. Rettig and S. Virtanen. Composition of corrosion layers on a magnesium rare-earth alloy in simulated body fluids. *Journal of biomedical materials research. Part A*, 88(2):359–69, February 2009.

[95] H. Altun and S. Sen. Studies on the influence of chloride ion concentration and pH on the corrosion and electrochemical behaviour of AZ63 magnesium alloy. *Materials & Design*, 25(7):637–643, October 2004.

[96] Y. Xin, K. Huo, H. Tao, G. Tang, et al. Influence of aggressive ions on the degradation behavior of biomedical magnesium alloy in physiological environment. *Acta biomaterialia*, 4(6):2008–15, November 2008.

[97] G. Song and S. Song. Corrosion behaviour of pure magnesium in a simulated body fluid. *Acta Physicochimica Sinica*, 2006.

[98] B. Shaw. Corrosion resistance of magnesium alloys. *ASM handbook*, 2003.

[99] L. Xu, E. Zhang, D. Yin, S. Zeng, et al. In vitro corrosion behaviour of Mg alloys in a phosphate buffered solution for bone implant application. *Journal of materials science. Materials in medicine*, 19(3):1017–25, March 2008.

[100] L. Yang and E. Zhang. Biocorrosion behavior of magnesium alloy in different simulated fluids for biomedical application. *Materials Science and Engineering: C*, 29(5):1691–1696, June 2009.

[101] E. Zhang, D. Yin, L. Xu, L. Yang, et al. Microstructure, mechanical and corrosion properties and biocompatibility of Mg–Zn–Mn alloys for biomedical application. *Materials Science and Engineering: C*, 29(3):987–993, April 2009.

[102] F. Witte, V. Kaese, H. Haferkamp, E. Switzer, et al. In vivo corrosion of four magnesium alloys and the associated bone response. *Biomaterials*, 26(17):3557–63, June 2005.

[103] L. Xu, G. Yu, E. Zhang, F. Pan, et al. In vivo corrosion behavior of Mg-Mn-Zn alloy for bone implant application. *Journal of biomedical materials research. Part A*, 83(3):703–11, December 2007.

[104] J. Lévesque, H. Hermawan, D. Dubé, and D. Mantovani. Design of a pseudo-physiological test bench specific to the development of biodegradable metallic biomaterials. *Acta biomaterialia*, 4(2):284–95, March 2008.

[105] A. Pardo, M. Merino, A. Coy, R. Arrabal, et al. Corrosion behaviour of magnesium/aluminium alloys in 3.5wt.% NaCl. *Corrosion Science*, 50(3):823–834, March 2008.

[106] A. Oyane, H.-M. Kim, T. Furuya, T. Kokubo, et al. Preparation and assessment of revised simulated body fluids. *Journal of biomedical materials research. Part A*, 65(2):188–95, May 2003.

[107] M. Marques. Simulated biological fluids with possible application in dissolution testing. *Dissolution Technol*, 18(3):15–28, 2011.

[108] S. Hiromoto, A. Yamamoto, N. Maruyama, H. Somekawa, et al. Influence of pH and flow on the polarisation behaviour of pure magnesium in borate buffer solutions. *Corrosion Science*, 50(12):3561–3568, December 2008.

[109] W. Ng, K. Chiu, and F. Cheng. Effect of pH on the in vitro corrosion rate of magnesium degradable implant material. *Materials Science and Engineering: C*, 30(6):898–903, July 2010.

[110] Y. Chen, S. Zhang, J. Li, Y. Song, et al. Dynamic degradation behavior of MgZn alloy in circulating m-SBF. *Materials Letters*, 64(18):1996–1999, September 2010.

[111] B. Liu and Y. F. Zheng. Effects of alloying elements (Mn, Co, Al, W, Sn, B, C and S) on biodegradability and in vitro biocompatibility of pure iron. *Acta biomaterialia*, 7(3):1407–20, March 2011.

[112] R. Krams, J. Wentzel, J. Oomen, R. Vinke, et al. Evaluation of Endothelial Shear Stress and 3D Geometry as Factors Determining the Development of Atherosclerosis and Remodeling in Human Coronary Arteries in Vivo : Combining 3D Reconstruction from Angiography and IVUS (ANGUS) with Computational Fluid Dyn. *Arteriosclerosis, Thrombosis and Vascular Biology*, 17(10):2061–2065, October 1997.

[113] P. Doriot and P. Dorsaz. In-vivo measurements of wall shear stress in human coronary arteries. *Coronary Artery Disease*, 11(6):495–502, 2000.

[114] J. J. Wentzel, D. M. Whelan, W. J. van der Giessen, H. M. van Beusekom, et al. Coronary stent implantation changes 3-D vessel geometry and 3-D shear stress distribution. *Journal of Biomechanics*, 33(10):1287–1295, October 2000.

[115] J. J. LaDisa, D. Hettrick, L. Olson, I. Guler, et al. Stent implantation alters coronary artery hemodynamics and wall shear stress during maximal vasodilation. *Journal of Applied Physiology*, 93(6):1939–46, 2002.

[116] J. Lévesque, D. Dubé, M. Fiset, and D. Mantovani. Investigation of Corrosion Behaviour of Magnesium Alloy AM60B-F under Pseudo-Physiological Conditions. In *Materials Science Forum*, volume 426-432, pages 521–526, July 2003.

[117] J. Yang, Y. Jiao, F. Cui, I.-S. Lee, et al. Modification of degradation behavior of magnesium alloy by IBAD coating of calcium phosphate. *Surface and Coatings Technology*, 202(22-23):5733–5736, August 2008.

[118] N. Li, C. Guo, Y. H. Wu, Y. F. Zheng, et al. Comparative study on corrosion behaviour of pure Mg and WE43 alloy in static, stirring and flowing Hank's solution. *Corrosion Engineering, Science and Technology*, 47(5):346–351, August 2012.

[119] C. Schille, M. Braun, H. Wendel, L. Scheideler, et al. Corrosion of experimental magnesium alloys in blood and PBS: A gravimetric and microscopic evaluation. *Materials Science and Engineering: B*, 176(20):1797–1801, December 2011.

[120] J. Geis-Gerstorfer, C. Schille, E. Schweizer, F. Rupp, et al. Blood triggered corrosion of magnesium alloys. *Materials Science and Engineering: B*, 176(20):1761–1766, December 2011.

[121] C. Schille, H.-P. Reichel, N. Hort, and J. Geis-Gerstorfer. Corrosion of experimental magnesium alloys for use as possible bone replacement material. In *Magnesium : 8th International Conference on Magnesium Alloys and their Applications*. Wiley-VCH, 2010.

[122] S. Zhang, X. Zhang, C. Zhao, J. Li, et al. Research on an Mg-Zn alloy as a degradable biomaterial. *Acta biomaterialia*, 6(2):626–40, February 2010.

[123] M. Schinhammer, A. C. Hänzi, J. F. Löffler, and P. J. Uggowitzer. Design strategy for biodegradable Fe-based alloys for medical applications. *Acta biomaterialia*, 6(5):1705–13, May 2010.

[124] E. Zhang, W. He, H. Du, and K. Yang. Microstructure, mechanical properties and corrosion properties of Mg–Zn–Y alloys with low Zn content. *Materials Science and Engineering: A*, 488(1-2):102–111, August 2008.

[125] Gamry Instruments. Basics of Electrochemical Corrosion Measurements, www.gamry.com/application-notes/basics-of-electrochemical-corrosion-measurements, 2014.

[126] W. Lorenz and F. Mansfeld. Determination of corrosion rates by electrochemical DC and AC methods. *Corrosion Science*, 21(9-10):647–672, January 1981.

[127] C. Yfantis, D. Yfantis, J. Anastassopoulou, T. Theophanides, et al. In vitro corrosion behavior of new magnesium alloys for bone regeneration. *Proceedings of the 5th WSEAS International Conference on Environment, Ecosystems and Development*, 2006.

[128] G. Song, A. Atrens, and D. S. John. A hydrogen evolution method for the estimation of the corrosion rate of magnesium alloys. *Proceedings Magnesium Technology 2001*, 2001.

[129] E. Zhang and L. Yang. Microstructure, mechanical properties and bio-corrosion properties of Mg–Zn–Mn–Ca alloy for biomedical application. *Materials Science and Engineering: A*, 497(1-2):111–118, December 2008.

[130] N. Kirkland, J. Lespagnol, N. Birbilis, and M. Staiger. A survey of bio-corrosion rates of magnesium alloys. *Corrosion Science*, 52(2):287–291, February 2010.

[131] H. S. Brar, J. Wong, and M. V. Manuel. Investigation of the mechanical and degradation properties of Mg-Sr and Mg-Zn-Sr alloys for use as potential biodegradable implant materials. *Journal of the mechanical behavior of biomedical materials*, 7:87–95, March 2012.

[132] X. Zhang, G. Yuan, L. Mao, J. Niu, et al. Effects of extrusion and heat treatment on the mechanical properties and biocorrosion behaviors of a Mg-Nd-Zn-Zr alloy. *Journal of the mechanical behavior of biomedical materials*, 7:77–86, March 2012.

[133] P. Lu, H. Fan, Y. Liu, L. Cao, et al. Controllable biodegradability, drug release behavior and hemocompatibility of PTX-eluting magnesium stents. *Colloids and surfaces. B, Biointerfaces*, 83(1):23–8, March 2011.

[134] P. Lu, L. Cao, Y. Liu, X. Xu, et al. Evaluation of magnesium ions release, biocorrosion, and hemocompatibility of MAO/PLLA-modified magnesium alloy WE42. *Journal of biomedical materials research. Part B, Applied biomaterials*, 96(1):101–9, January 2011.

[135] M. Guo, L. Cao, P. Lu, Y. Liu, et al. Anticorrosion and cytocompatibility behavior of MAO/PLLA modified magnesium alloy WE42. *Journal of materials science. Materials in medicine*, 22(7):1735–40, July 2011.

[136] L. Xu and A. Yamamoto. In vitro degradation of biodegradable polymer-coated magnesium under cell culture condition. *Applied Surface Science*, 258(17):6353–6358, June 2012.

[137] F. Singer, T. Distler, and S. Virtanen. Long-term Corrosion Behavior of Poly-L-lactic Acid Coated Magnesium in Dulbecco's Modified Eagle Medium at Body Temperature. *Int. J. Electrochem. Sci*, 2014.

[138] H. M. Wong, K. W. K. Yeung, K. O. Lam, V. Tam, et al. A biodegradable polymer-based coating to control the performance of magnesium alloy orthopaedic implants. *Biomaterials*, 31(8):2084–96, March 2010.

[139] L. Xu, F. Pan, G. Yu, L. Yang, et al. In vitro and in vivo evaluation of the surface bioactivity of a calcium phosphate coated magnesium alloy. *Biomaterials*, 30(8):1512–23, March 2009.

[140] M. B. Kannan and L. Orr. In vitro mechanical integrity of hydroxyapatite coated magnesium alloy. *Biomedical materials (Bristol, England)*, 6(4):045003, August 2011.

[141] E. Zhang, L. Xu, and K. Yang. Formation by ion plating of Ti-coating on pure Mg for biomedical applications. *Scripta Materialia*, 53(5):523–527, September 2005.

[142] A. Drynda, T. Hassel, R. Hoehn, A. Perz, et al. Development and biocompatibility of a novel corrodible fluoride-coated magnesium-calcium alloy with improved degradation kinetics and adequate mechanical properties for cardiovascular applications. *Journal of biomedical materials research. Part A*, 93(2):763–75, May 2010.

[143] Y. Al-Abdullat, S. Tsutsumi, N. Nakajima, M. Ohta, et al. Surface Modification of Magnesium by NaHCO3 and Corrosion Behavior in Hank's solution for New Biomaterial Applications. *Materials Transactions*, 42(8):1777–1780, September 2001.

[144] L. Li, J. Gao, and Y. Wang. Evaluation of cyto-toxicity and corrosion behavior of alkali-heat-treated magnesium in simulated body fluid. *Surface and Coatings Technology*, 185(1):92–98, July 2004.

[145] R. Walter and M. B. Kannan. Influence of surface roughness on the corrosion behaviour of magnesium alloy. *Materials & Design*, 32(4):2350–2354, April 2011.

[146] N. Birbilis, K. D. Ralston, S. Virtanen, H. L. Fraser, et al. Grain character influences on corrosion of ECAPed pure magnesium. *Corrosion Engineering, Science and Technology*, 45(3):224–230, June 2010.

[147] K. Ralston, N. Birbilis, and C. Davies. Revealing the relationship between grain size and corrosion rate of metals. *Scripta Materialia*, 63(12):1201–1204, December 2010.

[148] L. Petrini, F. Migliavacca, F. Auricchio, and G. Dubini. Numerical investigation of the intravascular coronary stent flexibility. *Journal of biomechanics*, 37(4):495–501, April 2004.

[149] P. Zunino, C. D'Angelo, L. Petrini, C. Vergara, et al. Numerical simulation of drug eluting coronary stents: Mechanics, fluid dynamics and drug release. *Computer*

Methods in Applied Mechanics and Engineering, 198(45-46):3633–3644, September 2009.

[150] D. Martin and F. J. Boyle. Computational structural modelling of coronary stent deployment: A review. *Computer methods in biomechanics and biomedical engineering*, 14(4):331–48, April 2011.

[151] S. Morlacchi and F. Migliavacca. Modeling stented coronary arteries: Where we are, where to go. *Annals of biomedical engineering*, 41(7):1428–44, July 2013.

[152] J. X. Jia, G. Song, A. Atrens, D. St John, et al. Evaluation of the BEASY program using linear and piecewise linear approaches for the boundary conditions. *Materials and Corrosion*, 55(11):845–852, November 2004.

[153] J. X. Jia, G. Song, and A. Atrens. Influence of geometry on galvanic corrosion of AZ91D coupled to steel. *Corrosion Science*, 48(8):2133–2153, August 2006.

[154] J. Jia, G. Song, and A. Atrens. Experimental Measurement and Computer Simulation of Galvanic Corrosion of Magnesium Coupled to Steel. *Advanced Engineering Materials*, 9(1-2):65–74, February 2007.

[155] Z. Shi, J. X. Jia, and A. Atrens. Galvanostatic anodic polarisation curves and galvanic corrosion of high purity Mg in 3.5% NaCl saturated with Mg(OH)2. *Corrosion Science*, 60:296–308, July 2012.

[156] K. B. Deshpande. Validated numerical modelling of galvanic corrosion for couples: Magnesium alloy (AE44)–mild steel and AE44–aluminium alloy (AA6063) in brine solution. *Corrosion Science*, 52(10):3514–3522, October 2010.

[157] J. Xiao and S. Chaudhuri. Predictive modeling of localized corrosion: An application to aluminum alloys. *Electrochimica Acta*, 56(16):5630–5641, June 2011.

[158] Y. Onishi, J. Takiyasu, K. Amaya, H. Yakuwa, et al. Numerical method for time-dependent localized corrosion analysis with moving boundaries by combining the finite volume method and voxel method. *Corrosion Science*, 63:210–224, October 2012.

[159] W. Sun, G. Liu, L. Wang, T. Wu, et al. An arbitrary Lagrangian–Eulerian model for studying the influences of corrosion product deposition on bimetallic corrosion. *Journal of Solid State Electrochemistry*, 17(3):829–840, November 2012.

[160] L. Kachanov. *Introduction to continuum damage mechanics*. Springer Netherlands, 1986.

[161] J. Lemaitre and H. Lippmann. *A course on damage mechanics*. Springer Berlin Heidelberg, 1996.

[162] J. Lemaitre and R. Desmorat. *Engineering damage mechanics: ductile, creep, fatigue and brittle failures*. Springer-Verlag Berlin Heidelberg, 2005.

[163] V. Bolotin and A. Shipkov. Mechanical aspects of corrosion fatigue and stress corrosion cracking. *International Journal of Solids and Structures*, 38(40-41):7297–7318, October 2001.

[164] H. da Costa-Mattos, I. Bastos, and J. Gomes. A simple model for slow strain rate and constant load corrosion tests of austenitic stainless steel in acid aqueous solution containing sodium chloride. *Corrosion Science*, 50(10):2858–2866, October 2008.

[165] M. Wenman, K. Trethewey, S. Jarman, and P. Chard-Tuckey. A finite-element computational model of chloride-induced transgranular stress-corrosion cracking of austenitic stainless steel. *Acta Materialia*, 56(16):4125–4136, September 2008.

[166] D. Gastaldi, V. Sassi, L. Petrini, M. Vedani, et al. Continuum damage model for bioresorbable magnesium alloy devices - Application to coronary stents. *Journal of the mechanical behavior of biomedical materials*, 4(3):352–65, April 2011.

[167] W. Wu, S. Chen, D. Gastaldi, L. Petrini, et al. Experimental data confirm numerical modeling of the degradation process of magnesium alloys stents. *Acta biomaterialia*, 9(10):8730–9, November 2013.

[168] W. Wu, L. Petrini, D. Gastaldi, T. Villa, et al. Finite element shape optimization for biodegradable magnesium alloy stents. *Annals of biomedical engineering*, 38(9):2829–40, September 2010.

[169] W. Wu, D. Gastaldi, K. Yang, L. Tan, et al. Finite element analyses for design evaluation of biodegradable magnesium alloy stents in arterial vessels. *Materials Science and Engineering: B*, 176(20):1733–1740, December 2011.

[170] N. Debusschere, M. De Beule, P. Segers, B. Verhegghe, et al. Modeling of Coated Biodegradable Stents, Proceedings of the ASME 2012 Summer Bioengineering Conference, 2012.

[171] J. A. Grogan, S. B. Leen, and P. E. McHugh. Optimizing the design of a bioabsorbable metal stent using computer simulation methods. *Biomaterials*, 34(33):8049–60, November 2013.

[172] J. A. Grogan, S. B. Leen, and P. E. McHugh. A physical corrosion model for bioabsorbable metal stents. *Acta biomaterialia*, 10(5):2313–22, May 2014.

[173] J. Chessa, P. Smolinski, and T. Belytschko. The extended finite element method (XFEM) for solidification problems. *International Journal for Numerical Methods in Engineering*, 53(8):1959–1977, March 2002.

[174] Y. Onuma and P. W. Serruys. Bioresorbable scaffold: the advent of a new era in percutaneous coronary and peripheral revascularization? *Circulation*, 123(7):779–97, February 2011.

[175] A. Hänzi. *Development of bioabsorbable magnesium alloys as implant material for vascular intervention*. PhD thesis, Swiss Federal Institute of Technology Zurich, 2009.

[176] S. Garg and P. Serruys. Biodegradable stents and non-biodegradable stents. *Minerva cardioangiologica*, 57(5):537–65, October 2009.

[177] R. Alexy and D. Levi. Materials and Manufacturing Technologies Available for Production of a Pediatric Bioabsorbable Stent. *BioMed research international*, 2013.

[178] E. Wittchow, N. Adden, J. Riedmüller, C. Savard, et al. Bioresorbable drug-eluting magnesium-alloy scaffold: Design and feasibility in a porcine coronary model. *EuroIntervention*, 8(12):1441–50, April 2013.

[179] D. Gastaldi, V. Sassi, L. Petrini, M. Vedani, et al. Continuum Damage Model for Biodegradable Magnesium Alloy Stent. *Advanced Materials Research*, 138:85–91, November 2010.

[180] M. De Beule, P. Mortier, S. G. Carlier, B. Verhegghe, et al. Realistic finite element-based stent design: The impact of balloon folding. *Journal of biomechanics*, 41(2):383–9, January 2008.

[181] W. Schmidt, P. Behrens, and K.-P. Schmitz. World Congress on Medical Physics and Biomedical Engineering. 25:136–139, 2009.

[182] Machine Solutions, www.machinesolutions.com/Medical-Device-Performance-Testing/Testing-Equipment/Radial-Expansion-Force-Testing-Equipment-RX550-650.htm, 2012.

[183] F. Harewood and P. McHugh. Modeling of size dependent failure in cardiovascular stent struts under tension and bending. *Annals of Biomedical Engineering*, 35(9):1539–1553, 2007.